Titre: Title:	Prediction of the Postoperative Shape of the Trunk After Spinal Surgery Using Deep Learning
Auteur: Author:	Siddhika Arunachalam
Date:	2024
Type:	Mémoire ou thèse / Dissertation or Thesis
Référence: Citation:	Arunachalam, S. (2024). Prediction of the Postoperative Shape of the Trunk After Spinal Surgery Using Deep Learning [Mémoire de maîtrise, Polytechnique Montréal]. PolyPublie. https://publications.polymtl.ca/58306/

URL de PolyPublie: PolyPublie URL:	https://publications.polymtl.ca/58306/
Directeurs de recherche: Advisors:	Farida Cheriet, François Guibault, & Marie Beauséjour
Programme: Program:	Génie informatique

POLYTECHNIQUE MONTRÉAL

affiliée à l'Université de Montréal

Prediction of the Postoperative Shape of the Trunk after Spinal Surgery using Deep Learning

SIDDHIKA ARUNACHALAM

Département de génie informatique et génie logiciel

Mémoire présenté en vue de l'obtention du diplôme de *Maîtrise ès sciences appliquées*

Génie informatique

Avril 2024

POLYTECHNIQUE MONTRÉAL

affiliée à l'Université de Montréal

Ce mémoire intitulé :

Prediction of the Postoperative Shape of the Trunk after Spinal Surgery using Deep Learning

présenté par **Siddhika Arunachalam**

en vue de l'obtention du diplôme de *Maîtrise ès sciences appliquées*

a été dûment accepté par le jury d'examen constitué de :

Lama SÉOUD, présidente
Farida CHERIET, membre et directrice de recherche
François GUIBAULT, membre et codirecteur de recherche
Marie BEAUSÉJOUR , membre et codirectrice de recherche
Jonathan BOISVERT, membre externe

DEDICATION

To my parents...

ACKNOWLEDGEMENTS

I would like to express my heartfelt gratitude to my supervisor, Prof. Farida Cheriet, for providing me with the opportunity to work under her guidance and for her invaluable constant support, and mentorship throughout my research journey. I am also thankful to my co-supervisors, Prof. Francois Guibault and Prof. Marie Beausejour for their constant support and motivation. Their expertise and insightful feedback have been instrumental in shaping my work and helping me navigate the complexities of my research topic.

I also wanted to extend a special thanks to Philippe Debanné for his support, availability, and for sharing his valuable insights into research studies and gathering datasets of AIS patients. His assistance was instrumental in the implementation of the project.

I would also like to extend my thanks to all the members of the LIV4D lab at École Polytechnique of Montreal for their insightful feedback and willingness to share knowledge.

Finally, I would like to thank my parents for their continued support and encouragement throughout my journey.

RÉSUMÉ

La scoliose idiopathique de l'adolescent (SIA) est une déformation complexe de la colonne vertébrale qui nécessite souvent une intervention chirurgicale. Une prédiction précise de la forme du tronc postopératoire est cruciale pour la planification chirurgicale et la satisfaction du patient. Cette recherche présente une approche d'apprentissage profond pour prédire la forme du tronc postopératoire chez les patients subissant une chirurgie de la scoliose. En utilisant une architecture d'apprentissage profond, où PointNet++ est considéré comme l'épine dorsale du modèle, nous avons développé un modèle d'apprentissage profond capable de traiter les données de topographie de surface du tronc complet (FBST) pour estimer la forme du tronc postopératoire à partir de données de nuage de points préopératoires. La méthodologie englobe le prétraitement des données, la conception de l'architecture du modèle, la formulation de la fonction de perte et les processus de validation, en mettant l'accent sur la capture des caractéristiques locales et globales de la forme du tronc. Nos résultats, basés sur un ensemble de données de patients atteints de scoliose idiopathique de l'adolescent (SIA), démontrent l'efficacité du modèle à prédire avec précision la forme du tronc postopératoire et sa validité par des mesures quantitatives comme la distance de Chamfer et des indices cliniques tels que la rotation de la surface dorsale et la rotation du tronc. L'étude d'ablation souligne l'importance d'incorporer la perte de forme, la perte de densité et la perte de lissage dans la fonction de perte du modèle pour obtenir des reconstructions réalistes. Une expérience de validation croisée k-fold soutient en outre la fiabilité du modèle à travers divers segments de données. Malgré les défis de capturer les détails anatomiques fins, nos résultats suggèrent un potentiel pour améliorer la planification chirurgicale et les résultats pour les patients. Les travaux futurs devraient explorer les entrées multimodales pour aborder les limitations actuelles et affiner davantage les prédictions.

ABSTRACT

Adolescent Idiopathic Scoliosis (AIS) is a complex spinal deformity that often requires surgical intervention. Accurate prediction of postoperative trunk shape is crucial for surgical planning and patient satisfaction. This research presents a deep learning approach to predicting the postoperative shape of the trunk in patients undergoing scoliosis surgery. Utilizing a deep learning architecture, where PointNet++ is considered as the backbone of the model, we developed a deep learning model capable of processing Full Body Surface Topography (FBST) data to estimate postoperative trunk shape from preoperative point cloud data. The methodology encompasses data preprocessing, model architecture design, loss function formulation, and validation processes, with a focus on capturing both local and global features of the trunk's shape. Our results, based on the dataset of Adolescent Idiopathic Scoliosis (AIS) patients, demonstrate the model's effectiveness in accurately predicting postoperative trunk shape and validating by quantitative metrics like Chamfer distance and clinical indices such as Back Surface Rotation and Trunk Rotation. The ablation study highlights the importance of incorporating shape loss, density loss, and smoothness loss in the model's loss function for achieving realistic reconstructions. A k-fold cross-validation experiment further supports the model's reliability across various data segments. Despite challenges in capturing fine anatomical details, our findings suggest potential for improving surgical planning and patient outcomes. Future work should explore multi-modal inputs to address current limitations and further refine predictions.

TABLE OF CONTENTS

LIST OF TABLES

LIST OF FIGURES

LIST OF SYMBOLS AND ABBREVIATIONS

AIS	Adolescent Idiopathic Scoliosis
BSR	Back Surface Rotation
CRD	Coronal Trunk Deviation
DA	Depth Asymmetry
STD	Sagittal Trunk Deviation
FBST	Full Body Surface Topography
TR	Trunk Rotation

CHAPTER 1 INTRODUCTION

Adolescent Idiopathic Scoliosis (AIS) is a condition that causes a complex 3D deformity of the trunk, affecting between 1 and 3% of the general population. The condition is characterized by an abnormal curvature of the spine, which can cause functional problems and asymmetries in the trunk shape [1]. Surgical correction of AIS is often necessary in most severe cases to stop the progression of the condition and to improve the patient's quality of life.

Every patient has a unique anatomy and a standardized surgical approach that may not be suitable for everyone. Advanced planning tools allow surgeons to customize their approach based on the individual characteristics of the patient, potentially leading to better outcomes. With improved surgical planning, outcomes become more predictable. Surgeons can foresee potential complications or challenges and take steps to mitigate them which helps reduce the uncertainty and risks associated with surgical interventions. An informed patient is more likely to have trust in the procedure and its outcome. Visualization and simulation tools can provide patients with a clearer understanding of the surgery, its implications, and its expected outcomes, thus setting realistic expectations [2].

Aubin et al. [3] had proposed a spine surgery simulator which is reliable, user-friendly, and safe to predict the correction of scoliosis spine deformity after surgery. This surgeon-friendly simulator provided advanced spinal surgery planning which works based on both patient’s characteristics and different instrumentation configurations. However, they had not investigated the correction of the external shape of the trunk after spinal surgery.

Predicting the post-surgery external appearance of the trunk holds significant importance in the context of spine surgeries. One primary reason is patient expectations and satisfaction. It can help clinicians to plan the surgery better, set realistic expectations for the patient, and decide on the best course of action. Patients can also understand the potential benefits and risks of the surgery and make an informed decision about whether to proceed with the surgery or not. Many patients opt for spine surgeries not solely for the functional enhancements but also by giving importance to aesthetic improvements. They hope for a shift towards a more balanced and conventional trunk

appearance. Achieving a symmetrical appearance can have profound positive implications on a patient's self-esteem, psychological health, and overall life quality[4] [5].

Furthermore, by understanding the impact of various surgical interventions on the external trunk appearance, surgeons can refine and adapt their techniques to ensure better overall results. It may lead to the development of newer methods or modifications to existing ones to address these aesthetic concerns [6].

Although, in the field of orthopedic surgery, accurately predicting the outcome of a surgical intervention can be challenging. This is particularly true for scoliosis surgery, where the surgeon must correct the curvature of the spine while maintaining as much mobility and function as possible. Clinicians aim to treat patients with scoliosis to improve their spinal curvature and the external appearance of the trunk. However, predicting the outcome of treatment can be difficult for clinicians, which can lead to persisting external asymmetry of the trunk [7], [8]. Spinal surgery is a complex and invasive procedure that carries risks and potential complications, and it is, therefore, crucial to accurately predict the outcome of treatment to minimize these risks.

Also, without accurate prediction of the postoperative trunk surface, clinicians may have difficulty selecting the optimal surgical strategy and communicating with patients effectively about their treatment options. Additionally, communicating the potential outcomes of surgery to patients can be difficult, especially when relying on static images or verbal descriptions. Patients may not fully understand the impact that surgery will have on their mobility and function, which can lead to dissatisfaction with the results of the procedure.

Due to these reasons, we are motivated to leverage the capabilities of deep learning to accurately predict the postoperative shape of the trunk in patients undergoing corrective surgery for scoliosis. Additionally, the research seeks to evaluate the influence of various model loss components on its effectiveness which is also called ablation study. Furthermore, the study also aims to derive clinically significant metrics from the predicted postoperative shape to assess its alignment with expected surgical outcomes. Lastly, a quantitative validation of the predicted trunk shape is performed to ensure the model's reliability and accuracy in a clinical setting.

This thesis is structured as follows:

Chapter 2, titled "Background and Literature Review," provides a comprehensive overview of the existing research and developments in the field of scoliosis treatment, focusing on surgical interventions and the importance of predicting postoperative outcomes.

Chapter 3, "Methodology," details the approach taken in this study to design and implement a deep learning model for predicting the postoperative shape of the trunk in scoliosis patients.

Chapter 4, "Results and Discussion," presents the findings of the study, including the performance of the deep learning model in predicting postoperative trunk shape and the results of the ablation study.

Chapter 5, "Conclusion," summarizes the key findings of the study, discusses the limitations, and suggests directions for future research.

CHAPTER 2 BACKGROUND AND LITERATURE REVIEW

This chapter is organized as follows: Section 2.1 reviews the existing studies of assessing the surgery outcome and simulating the postoperative trunk and spine shapes. Section 2.2 reviews the state-of-art domain studies related to the prediction of the Scoliosis Surgery outcome using Machine Learning Approaches. Section 2.3 reviews various studies related to modeling of the trunk shape surface.

2.1 Adolescent Idiopathic Scoliosis

2.1.1 Definition

Scoliosis is a three-dimensional deformation of the spine, characterized by a lateral curvature in the frontal plane, a loss of physiological curvatures in the sagittal plane, rotation of the vertebrae in the axial plane, and local deformation of the vertebrae. In addition to spinal deformations, there is asymmetry in the rib cage [9] (see Figure 2.1).

Depending on the patient's age, idiopathic scoliosis can be classified as: infantile (0 - 4 years), juvenile (4 - 10 years), adolescent (10 - 18 years), or *de novo*, which affects adults after growth. In this study, we are interested in Adolescent Idiopathic Scoliosis (AIS), which affects more girls than boys with a ratio of 6:1. This ratio increases with the severity of scoliosis and can reach 10:1 for a Cobb angle of 30° [10]. The Cobb angle and the severities of scoliosis will be presented in the following paragraphs.

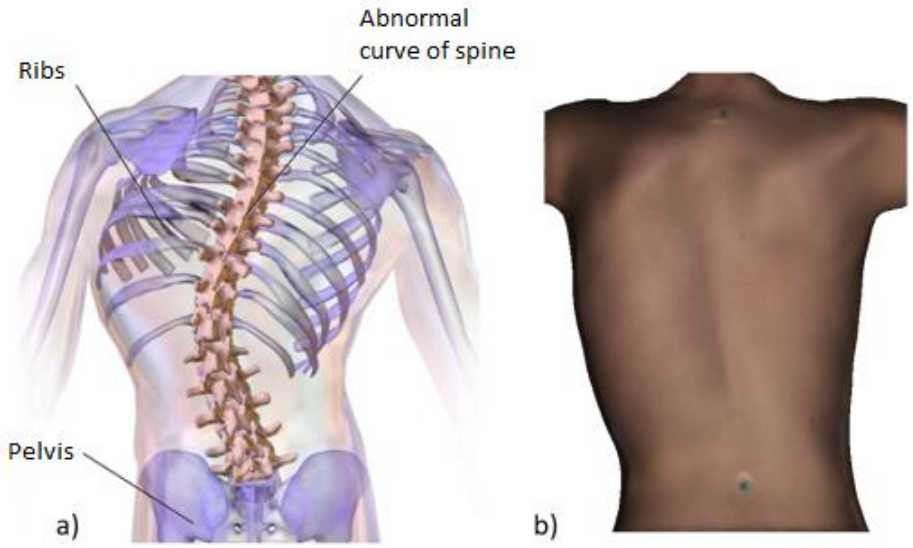

Figure 2.1 Posterior view of scoliosis. (a) Internal view (adapted from Bruce Blaus[1]), (b) external view[1]

AIS rarely causes pain. It is often visualized by asymmetry in the shoulders and hips, a hump on the back (gibbosity), a prominent shoulder blade caused by the rotation of the rib cage, a difference in sizes and heights of the breasts, and a difference in distance between the arms and the body [9]. These differences are increasingly perceived with the worsening of scoliosis severity. Physical deformations can be accompanied by psychosocial disorders such as low self-esteem, adolescent concerns about their body shape, a risk of depression, and alcohol consumption [11]. Untreated severe scoliosis can cause long-term respiratory and cardiac problems.

2.1.2 Evaluation

Clinical Evaluation

The clinical evaluation of Adolescent Idiopathic Scoliosis (AIS) relies on the visual assessment of asymmetries and deformations of the trunk. First, the patient is examined in a standing position from anterior, posterior, and lateral views. Asymmetries at the shoulders and pelvis are observed by checking the horizontality of the iliac crests; the prominence of one of the scapulae and the presence of an asymmetrical fold at the waist level. Viewed from the back, lateral displacement is

[1] Blausen.com staff (2014). "Medical gallery of Blausen Medical 2014". WikiJournal of Medicine. DOI :10.15347/wjm/2014.010. ISSN 2002-4436.

examined using a plumb line, which corresponds to the horizontal deviation of the trunk. A standing measurement using a plumb line stretched from the C7 vertebral prominence allows for quantification of the trunk's lateral displacement (Figure 2.2.b). The hump is evaluated using the Adams forward bend test, where the patient is asked to lean forward. In this position, the asymmetry of the back's contour becomes more visible. The hump, or rib hump, is a result of deformities in the costo-vertebral joints and the rotation of the vertebral bodies. To measure this hump quantitatively, a scoliometer is used. This instrument measures the degree of vertebral rotation in millimeters by being centered over the spine at the site of the most pronounced curvature [12], [13].

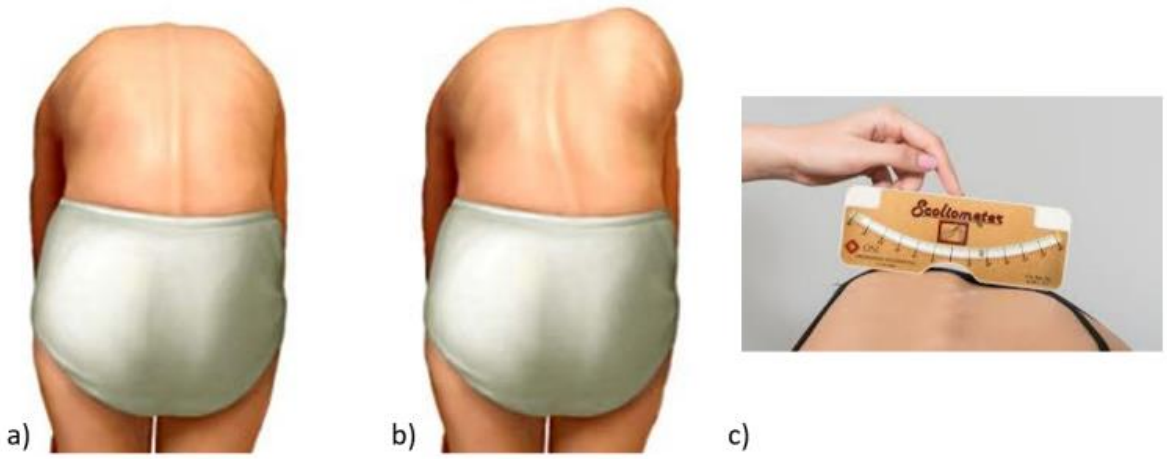

Figure 2.2 Adams test to evaluate the hump. (a) Healthy subject, (b) patient presenting a hump, (c) use of a scoliometer to quantify the hump[2]

Radiological Evaluation

To confirm a diagnosis of scoliosis, a radiological evaluation is performed. Two spinal radiographs are acquired, one frontal and one lateral in a standing position. The major Cobb angle, measured on the frontal radiograph, is the key metric for evaluating scoliosis severity. It is calculated by drawing lines tangent to the upper and lower endplates of the most tilted vertebrae at the top and bottom of the spinal curve, respectively. These vertebrae are known as the upper and lower limit vertebrae. The angle between these lines quantifies the lateral curvature of the spine in degrees

[2] photos taken from https://commons.wikimedia.org/wiki

which offers a standardized approach to diagnose scoliosis and monitor its progression or treatment response.

Sometimes the patient presents more than one curvature of the spine; in this case, additional Cobb angles can be measured to evaluate them. In the frontal plane, one to three curvatures can be distinguished, and consequently, 3 Cobb angles can be measured: the proximal thoracic Cobb angle (upper curvature of the spine), the major Cobb angle (middle curvature of the spine), and the lumbar Cobb angle (lower curvature of the spine). The angles are measured by considering the most inclined vertebrae and measuring the angle between the tangents to their endplates (see Figure 2.3). The position of the apical vertebra (the apex) defines the type of scoliosis; it is the vertebra most deviated from the center of the spine (see Figure 2.3). The scoliosis is thoracic when the apex is located between vertebrae T2 and T12, it is thoracolumbar when the apex is located between vertebrae T12 and L1, and it is lumbar when the apex is located between vertebrae L1 and L5.

In the sagittal plane, two natural curvatures are distinguished: thoracic kyphosis and lumbar lordosis. They are quantified by measuring the angle formed by the tangents to vertebrae T2 and L1 and the angle formed by the tangents to vertebrae L1 and L5, respectively.

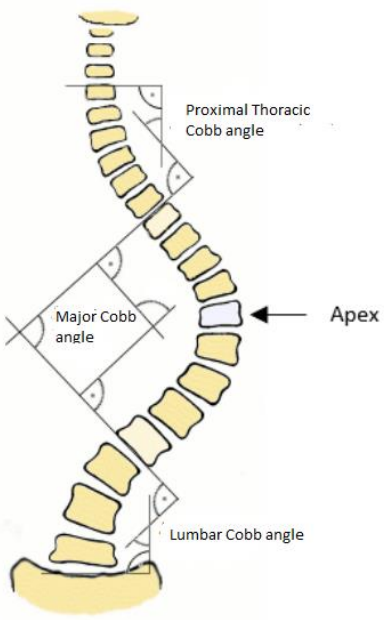

Figure 2.3 Frontal view of the spine illustrating the measurements of the thoracic, major, and lumbar Cobb angles (adapted from https://www.physio-pedia.com/)

A Cobb angle greater than 10° indicates the presence of scoliosis; its value reflects the severity of the deformation [14]:

- Mild scoliosis: 10° < Cobb angle < 15° - The patient does not undergo any treatment but must be monitored by their doctor.
- Moderate scoliosis: 20° < Cobb angle < 40° - A brace is recommended.
- Severe scoliosis: Cobb angle > 40° - Surgery is recommended.

Monitoring scoliosis requires radiographs every six months. Since the measurement of the Cobb angle on radiographs presents an error of 5°, a difference in Cobb angle greater than 5° between two exams indicates a progression of scoliosis [12] [15].

2.1.3 Treatment

As mentioned earlier, untreated scoliosis can progress and have serious consequences for the patient, such as pain, heart and respiratory problems, and psychological disorders.

The progression of scoliosis depends on several factors. One factor is the maturity of the patient, including their age at first diagnosis, bone maturity, and menstruation in girls. Bone maturity is assessed by a Risser test. The Risser index ranges from 0 to 5 based on the appearance and attachment of the growth cartilage of the iliac crest. A Risser = 0 indicates the absence of cartilage and therefore immaturity, while a Risser = 5 indicates that the cartilage is fully attached to the iliac crest and that the subject has reached bone maturity. Bone immaturity leads to a higher risk of progression of spinal deformity. Other factors that affect progression are the Cobb angle and the position of the apex. A greater curvature and a thoracic apex present a greater risk of progression [16].

Observation of these factors allows clinicians to decide which treatment to follow, as brace treatment stops the progression of scoliosis, while surgical treatment corrects the deformity.

Brace Treatment

Patients with moderate Adolescent Idiopathic Scoliosis (AIS) (20° < Cobb Angle < 40°) are treated with a brace. The brace does not correct scoliosis but stops the progression of spinal deformity

during growth. It reduces the risk of surgery in 75% of cases [17]. The brace is worn throughout the growth period until bone maturity is reached. If it is a daytime brace, it is prescribed for 18 to 23 hours a day. There are several types: the Boston brace, the Wilmington brace, the Cheneau brace, etc. In some cases, a nighttime brace is sufficient to limit the progression of the deformity. The patient must wear it for 8 to 12 hours a day, mainly in bed. There are also different types, such as the Providence brace and the Charleston brace. It is designed to exert pressure on the external surface of the patient's trunk. These pressures propagate through the soft tissues to the spine (see Figure 2.4). The brace is effective when worn for the entire designated period, which can be inconvenient for patients.

The classic method of designing braces is based on a 2D image: a posteroanterior radiograph, from which a design board (blueprint) is created. The brace is then made using a plaster mold of the patient's trunk shape, with pads added at pressure points according to the design board [18]. This technique has several limitations, mainly because it uses a 2D image for the treatment of a 3D deformation, and because the braces are uncomfortable for patients. The research team at CHUSJ has developed 3D reconstruction tools [19] [20] for the manufacture of braces customized to the geometry of patients' trunks.

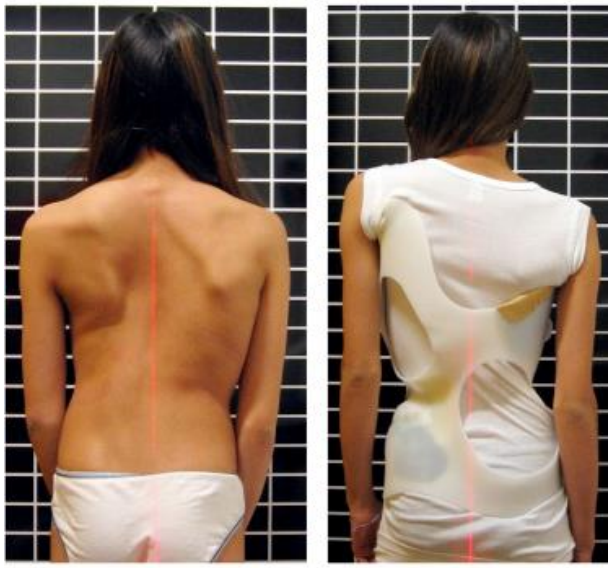

Figure 2.4 (Left) External deformation of the trunk of a patient with scoliosis, (Right) Brace worn by the same patient to treat the deformation (taken from Weiss HR[3])

Surgical Treatment:

Surgery is prescribed when the deformation of the spine worsens. If bone maturity has not been reached, the progression of scoliosis is rapid, and surgery is necessary for a Cobb angle greater than 40°. When bone maturity is completed, the progression is slower, and surgery is recommended when the Cobb angle reaches 50°.

The surgery involves straightening the spine using metal rods fixed with pedicle screws and hooks. Bone grafts are also introduced between the treated vertebrae to fuse them. This results in the reduction of the Cobb angle [21].

2.2 3D reconstruction of the spine from X-rays

The acquisition and 3D reconstruction of the spine for scoliosis assessment involve a standardized process using X-rays and specific imaging systems. At the Sainte-Justine Hospital Research Center in Montreal, Canada, patients undergoing scoliosis evaluation are imaged using a Fuji FCR7501S imaging system. The procedure involves taking two standard radiographs of the entire trunk in an

[3] Weiss HR. Scoliosis 2007, 2 :19. PMID : 18163917. doi :10.1186/1748-7161-2-19

upright position: one lateral (LAT) and one posteroanterior (PA). A rotary platform facilitates patient positioning from LAT to PA, while a stabilization device with elbow supports and handlebars minimizes involuntary movements during the X-ray acquisition [22].

For calibration purposes, patients wear a jacket with 16 embedded radio-opaque markers, and an external planar plate is used to define a global reference frame for subsequent 3D reconstructions. The radiographs undergo a non-linear optimization process for calibration, and anatomical landmarks are manually identified on each X-ray to reconstruct the vertebrae in 3D [23].

In the reconstruction process, six anatomical landmarks are manually identified for each vertebra in the X-ray images. These landmarks are then used to reconstruct the vertebrae in 3D, providing detailed patient-specific information about the geometry of each vertebra [24]. Generic vertebral models are subsequently adapted to fit each set of six reconstructed points, thereby completing the 3D geometry of each vertebra [25]. This process enables a detailed 3D representation of the spine, essential for accurate scoliosis assessment and treatment planning [9].

2.3 Trunk Shape Acquisition using Inspeck

For obtaining Full Body Surface Topography (FBST), the InSpeck system is used. InSpeck is a triangulation sensor, which is a type of 3D sensor that uses a camera to capture 3D images of an object. InSpeck is used to capture 3D images of the patient's trunk, providing a non-contact, non-invasive method of obtaining 3D images [26]. The InSpeck system is available at the CHU Sainte-Justine Hospital and consists of four serial digitizers, each of which includes a halogen structured light projector and a CCD camera. The system is capable of accurately capturing the shape and curvature of the patient's trunk surface in the standing posture. Figure 2.5 shows various steps involved in the Trunk topography measurement and reconstruction [8] [27] .

The trunk's surface geometry is captured using a system comprising four optical 3D digitizers from Creaform Inc., based in Levis, Canada. Each digitizer is equipped with a CCD camera and a structured light projector strategically positioned around the subject (refer to Figure 2.6). The acquisition process for each scanner involves projecting a set of fringe patterns onto the trunk's external surface and capturing the deformed patterns. The system employs triangulation to calculate the depth of each point on the surface relative to the digitizer's reference plane. A fifth

image is taken without fringes to provide texture information that is then mapped onto the surface model. The entire trunk geometry is obtained by registering and merging the partial surfaces obtained by each digitizer. This procedure requires the patient to remain stationary for approximately 4 to 6 seconds in a standing posture, with their arms slightly raised to minimize blind spots in the field of view of the lateral scanners. The final surface mesh produced consists of between 50,000 to 90,000 vertices [8].

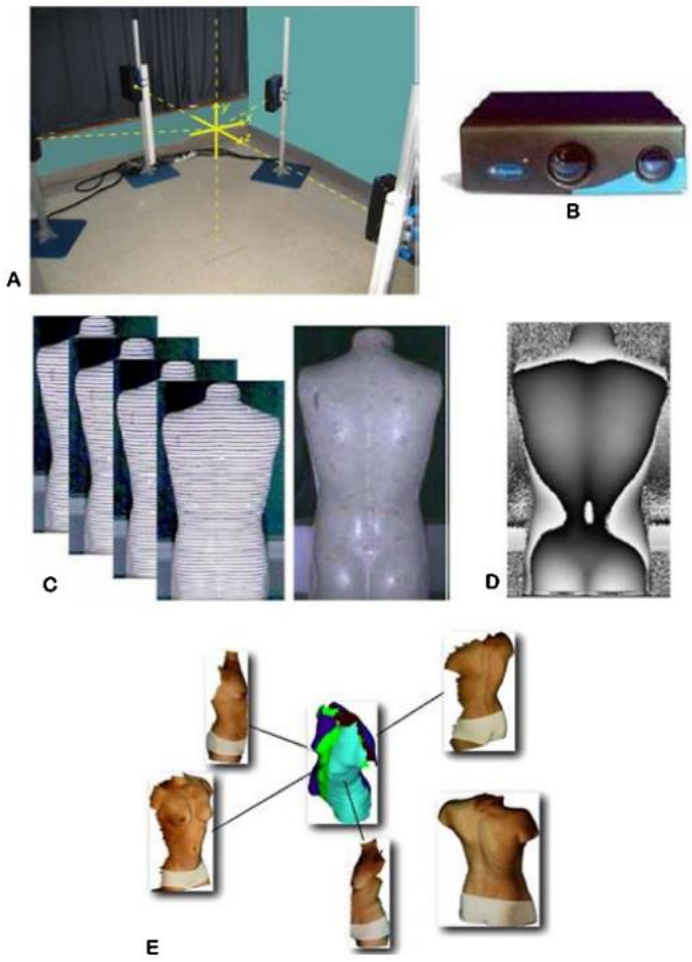

Figure 2.7 Trunk topography measurement and reconstruction A) Experimental set-up at Sainte-Justine Hospital of four Creaform optical digitizers. (B) Example of a Capturor II LF 3D optical digitizer, consisting of a CCD camera coupled with a structured light projector. (C) Set of four fringe images, each offset by 1/4 phase, projected by a digitizer onto the back of a mannequin; the fifth image provided the surface texture. (D) Resulting phase image from the four fringe images (E) The process of registering and merging the partial surfaces from the different digitizers produces the complete trunk surface

2.4 Trunk Shape Surface Modeling

The study by Valerie Pazos *et al.* [28] aimed to assess the reliability of 3D trunk surface measurements in characterizing external asymmetry related to scoliosis. The authors used repeated trunk surface acquisitions from patients attending a scoliosis clinic in two different postures. They computed a series of measurements for each acquisition and obtained intraclass correlation coefficients (ICC) for each measure and posture. The results showed fair to excellent reliability for posture A (anatomical position) and moderate to excellent reliability for posture B ("clavicle" position). Figure 2.8 shows partial surfaces obtained from the four digitizers, brought into a common coordinate system. The smallest detectable differences for maximal back surface and trunk rotation were also calculated. However, the authors noted that the system used in this study may not be sensitive enough to detect small changes in trunk shape over time, which could be a limitation for monitoring disease progression.

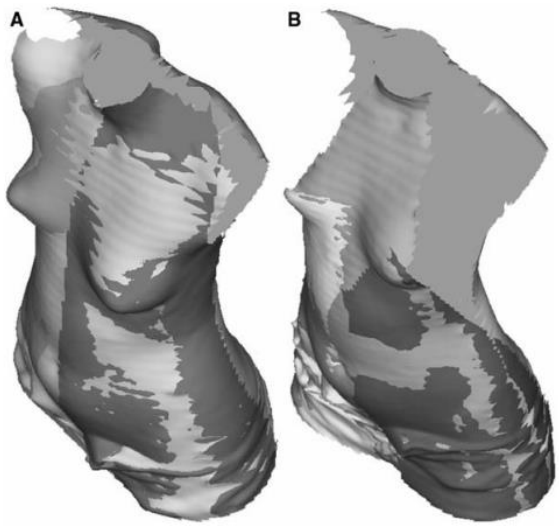

Figure 2.8 Surface coverage for posture A and B

The aim of the study by Lama Seoud *et al.* in [29] was to assess the reliability of a new set of multilevel trunk cross-section measurements for noninvasive assessment of trunk deformity in patients with adolescent idiopathic scoliosis (AIS). The study involved computing back surface rotation, trunk rotation, coronal and sagittal trunk deviation on 300 cross sections of the trunk and representing each set of 300 measures as a single functional data using a set of basis functions. The

study found good between-acquisition reliability at all trunk levels, indicating the potential usefulness of these measurements for monitoring progression and assessing treatment outcome in AIS patients. A functional correlation analysis also revealed the absence of redundancy between the measurements. Figure 2.9 shows the graphical user interface built for the visualization of the trunk 3D reconstruction, the trunk cross sections, and the four functional measurements. Although, the study did not assess the sensitivity of the multilevel trunk surface measurements for detecting small changes in scoliosis deformity, which is an important consideration for clinical monitoring and treatment evaluation. Additionally, the study did not evaluate the correlation of the new measurements with radiographic indices, which would be necessary for establishing their validity as a noninvasive assessment tool for scoliosis.

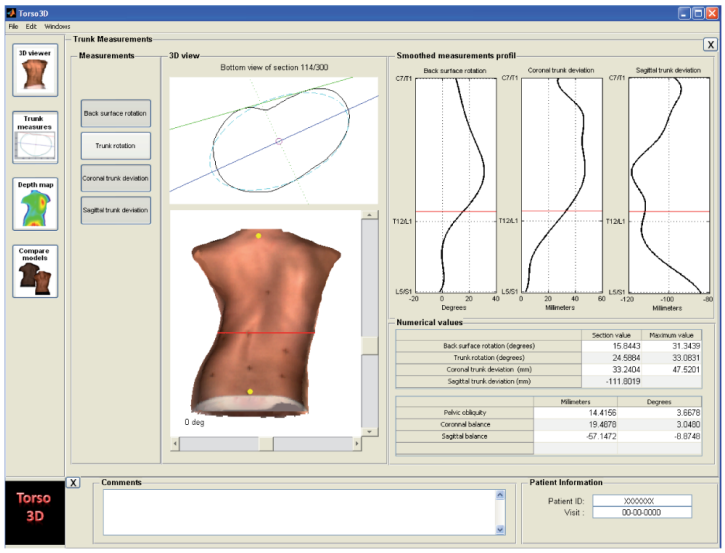

Figure 2.9 Graphical user interface for trunk measurements visualization.

The above limitation was overcome in this following study by Lama Seoud *et al.* in [30]. The paper proposed an objective method to quantify changes in trunk shape after scoliosis surgery using non-invasive optical system. Trunk shape was described by lateral deviation and axial rotation measurements, and a correction rate was computed for both measurements to assess pre and postoperative differences. The paper suggested that with the new quantitative trunk shape descriptor, clinicians and surgeons can objectively assess trunk deformity and postoperative shape, and proposed new treatment strategies that better address patients' concerns about their appearance. The study found that surgery achieved a very good correction of the lateral trunk deviation but only

a poor to moderate correction of the back axial rotation. This suggests that patients still face residual trunk deformity after surgery, mainly a persisting hump on the back.

2.5 Scoliosis Surgery Planning systems

The objective is to predict the postoperative shape of the trunk. Hence to achieve this, this topic provides a framework for planning and simulating surgical interventions.

Researchers have proposed biomechanical models of the spine's structure, particularly by Aubin *et al.* [3] [11]. These models enable simulations of spinal deformations and surgical corrections, as well as the planning of surgical instrumentation [3] [32], with predictable and reliable results.

The study in [3] aimed to develop and evaluate a spine surgery simulator called S3 for the preoperative planning and prediction of correction using different instrumentation configurations in scoliotic spines. A kinetic model using flexible mechanisms was developed to represent patient-specific spine geometry and flexibility and to simulate individual sub-steps of correction with an instrumentation system. The surgeon-friendly simulator interface allowed interactive specification of the instrumentation components, surgical correction maneuvers, and display of simulation results. The graphical user interface (GUI) of the Spine Surgery Simulator (S3) (Figure 2.10) was a high-level intuitive framework that was designed to guide the surgeons through the main steps of the virtual spinal instrumentation process without having to deal with the low-level computational aspects of the model. The simulations of spinal instrumentation procedures of 10 scoliotic cases agreed well with postoperative results and the expected behavior of the instrumented spine. (Figure 2.11) shows the outputs obtained through simulations from the preoperative to postoperative radiographs.

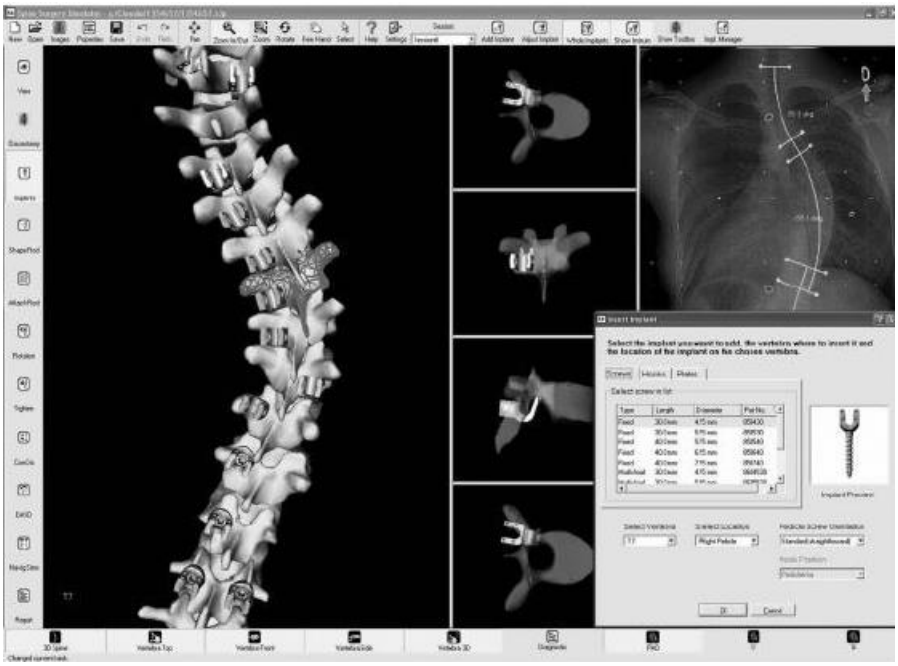

Figure 2.10 Graphical User Interface (GUI) of the spine surgery simulator (S3)

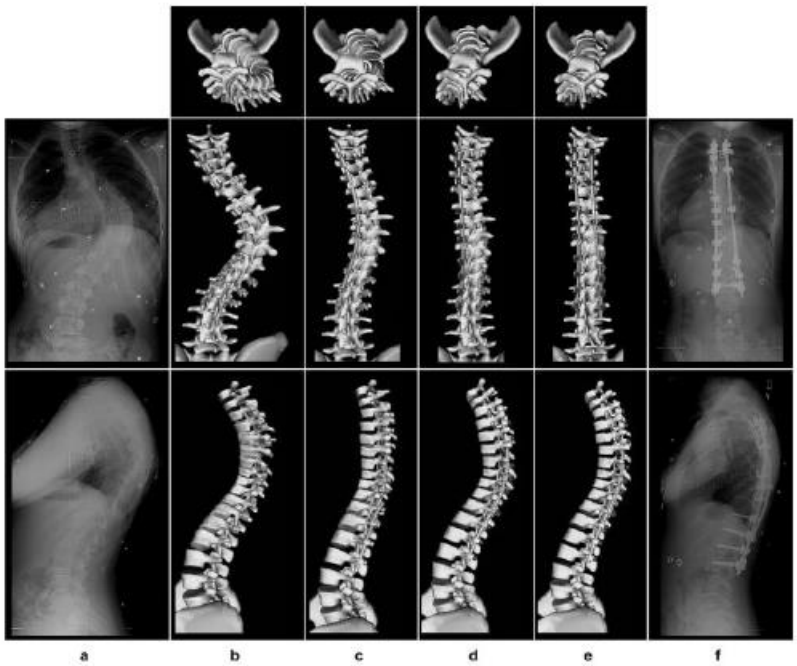

Figure 2.11 Representation of patient spine and instrumentation during a simulation

O. Dionne *et al.* [6] described a method for the scoliotic trunk shape prediction after a spine surgical intervention. A calibrated system consisting of 3D optical digitizers was used for obtaining surface geometry of the trunk. Then, the tetrahedral mesh generation of the trunk was performed. The trunk shape deformation model consisted of two transformations wherein, the first transformation is from the pre-to-postoperative sets of anatomical landmarks of spinal bone structures. The second transformation is the coordinate vector of mesh vertices corresponding to the soft tissue which uses the energy minimization method. The simulation results were described in Figure 2.12 where good approximation of rib hump correction was seen as a difference between the simulated and postoperative trunk surface. Although, some dissimilarities were observed in the upper portion of the back. Also, the proposed model did not consider the exact physical properties of the trunk soft tissue as the tissue elastic properties vary according to the type of scoliosis.

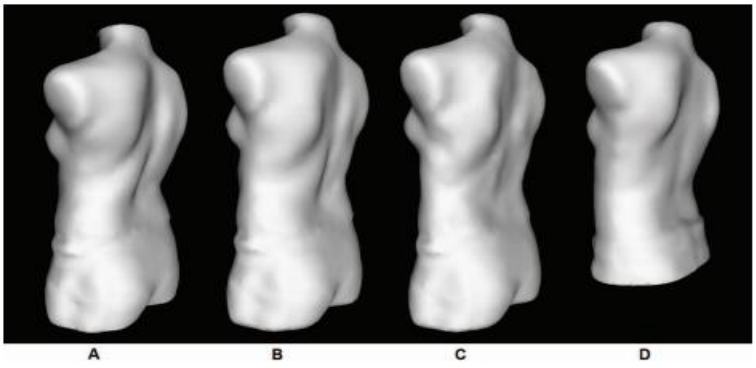

Figure 2.12 Simulation results

The above mentioned research [6] was followed-up by K. C. Assi *et al.* [33] where they proposed a novel incremental approach for the postoperative trunk shape simulation. The trunk surface topography and the 3D geometry reconstruction of the trunk's bone structures were acquired by the non-invasive active vision system and a calibrated bi-planar X-ray imaging system. To keep the linear elastic behavior of the soft tissue properties, their incremental method reduced the large nonlinear deformities into a set of small deformities. Figure 2.13 shows its flowchart and simulation results. This postoperative trunk shape simulator helped find the optimal scoliosis surgery strategy by considering the outcome of surgery on the external shape of the trunk. The simulation results shown in Figure 2.14 that the region of the back (spine) was produced well. From, the BSR indices, the simulated trunks were quantitatively close to the actual postoperative trunk surfaces which was also maintained in the qualitative comparison. However, some discrepancies in the upper region of

the back and a rib hump were still observable on the simulated trunk surface as compared to the actual postoperative trunk surface. The possible reasons for these discrepancies were assumed to be effect of posture, i.e. differences in standing posture between the pre and postoperative trunk acquisitions along with another possible factor such as weight change (i.e loss or gain) between the preoperative and postoperative acquisitions.

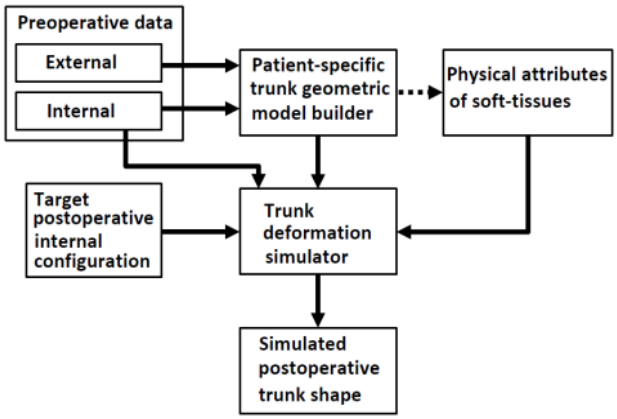

Figure 2.13 Flow chart o f the postoperative trunk shape simulation

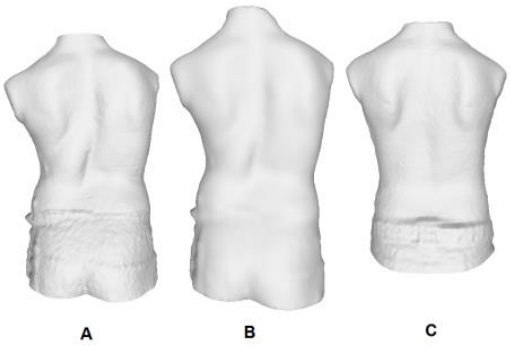

Figure 2.14 Example of simulation results

The paper by Robitaille *et al.* in [32] discussed about the decision-making process involved in scoliosis surgery with the introduction of new spinal fixation devices and preoperative corrective maneuvers. The authors aimed to evaluate the biomechanical effects of different instrumentation strategies on scoliotic cases. They simulated several strategies suggested by surgeons for five cases

using a spine surgery simulator. The study found that the average correction was better with pedicle screws than with hooks and hybrid constructs. However, this study questions the criteria for optimal configuration and standards to design the best surgical construct.

The aim of the study by Majdouline *et al.* in [34] was to use a computer model implemented in a spine surgery simulator to develop a method for defining the optimal surgical instrumentation strategy. The study simulated 702 different strategies on a scoliotic patient and assessed each configuration using objective functions representing different correction objectives. Figure 3 shows the flowchart of the materials and methods used to optimize instrumentation strategy. The results showed that the optimal strategy could be located using an interpolation technique, and that fewer implants (only screws) and less instrumented levels could achieve the same overall correction. Figure 2.16 shows the resulting correction and optimal instrumentation configuration obtained from the simulation. The study demonstrated the potential and feasibility of using a spine surgery simulator to optimize the planning of surgical instrumentation in AIS.

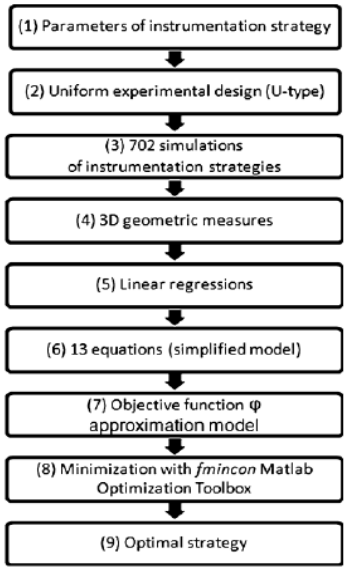

Figure 2.15 Flow chart summarizing the Materials and Methods

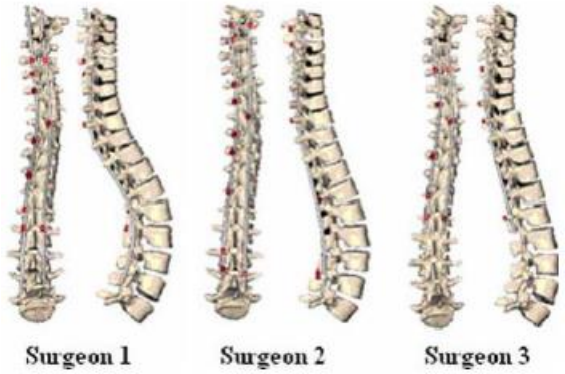

Figure 2.16 Resulting correction and optimal instrumentation configuration

Significant studies to date have focused on the effect of treatments on the spine and modeling the impact of braces on bone structure [35]. Other research has explored the modeling and simulation of rib surgery [36], which is a surgical procedure to correct a deformity in the ribcage. These studies have contributed to advancing our understanding of the spine's biomechanics and have helped improve the effectiveness of surgical interventions.

A study described in [36] developed a biomechanical model to evaluate the long-term correction resulting from the shortening or lengthening of ribs in adolescent idiopathic scoliosis. To simulate rib surgery, the researchers used a finite element model of the trunk, which was customized to the

geometry of a patient. The model also integrated several factors, such as the stress relaxation of ligament following surgery, the longitudinal growth of vertebral bodies and ribs, and their modulation due to mechanical stresses. The study found that the shortening of the slope on the concavity could potentially result in long-term correction of the column curvature. Overall, this study provides valuable insights into the biomechanics of scoliosis and the potential effectiveness of rib surgery as a treatment option.

D Périé *et al.* in [35] elaborated the development of a simulation tool for the design and evaluation of scoliosis brace treatment. This tool used a finite element model of a brace and its interface with the torso, which was adapted to represent a teenage girl with scoliosis treated with the Boston brace. The model included osseo-ligamentous structures, thoracic and abdominal soft tissues, a pad and shell, and the brace-torso interface. This study demonstrated the tool's ability to more realistically represent the transfer of load from the brace to the spine through various intermediate tissues. Other recent work by Clin *et al.* [37], [38], [39], [40], [41] has focused on various types of braces and their biomechanical influence and corrective effects on the spine or bone structure. These studies contribute to our understanding of the effectiveness of different types of braces for scoliosis treatment and how they impact the biomechanics of the spine.

In [42], the development of a biomechanical model of the human trunk was described to model and simulate trunk lateral bending tests. These tests are commonly used to evaluate scoliotic patients before surgery, in order to assess spinal curvatures, their flexibility, and potential for correction. The model included the osseo-ligamentous components of the vertebral column, the thoracic cage, the pelvis, and 160 muscle bundles represented by bilinear cable elements. The authors were able to accurately represent the modification of the thoracic Cobb angle, with an error of less than 2 degrees, as well as the projections of vertebral rotations in the frontal plane, with an accuracy of over 85%. They also achieved an adequacy greater than 77% in representing the positions of the centroids of the vertebral bodies. This study provides valuable insights into the biomechanics of scoliosis and the potential for using simulation models to accurately evaluate and plan surgical interventions.

The previous studies mentioned above have primarily focused on the effects of scoliosis correction on bone structure, without addressing the prediction of the postoperative external appearance of the patient's trunk.

2.6 Physics-based Deep Learning Architectures

A deep learning model for fast prediction of soft-tissue deformation in orthognathic surgical planning was proposed by Lampen et al. in [43]. It is motivated by the limitations of the finite element method (FEM) for predicting facial deformation due to its high computational cost. The authors proposed a novel deep neural network based on the PointNet++ architecture that accepts point cloud data and explicit boundary types as inputs for predicting soft-tissue deformation. Figure 2.17 shows the method that was proposed for the prediction of facial mesh displacement using Facial Mesh Coordinates and Bone Surface displacements as inputs and predicted Facial Mesh Displacements by using PointNet++ network. Facial meshes were generated using their already validated FEM simulated method. One of the main limitations of their work was that they only used Mean Squared Error (MSE) as the loss function. Also, from [44] they realized that shape inaccuracies resulted when simulating hyper-elastic materials due to the use of MSE as the loss function. However, incorporating a smoothing loss algorithm could potentially address visual accuracy concerns as also suggested by them.

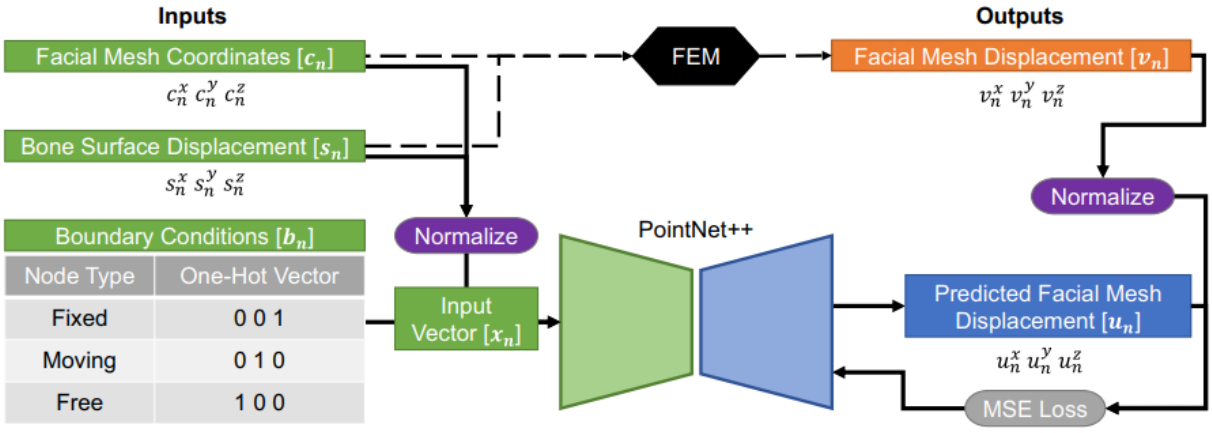

Figure 2.17 Overview of the method used for the deformation prediction

A biomechanically-trained deep learning model was presented in [45] to predict prostate motion during ultrasound-guided interventions. Using PointNet, the model was trained using finite element (FE) simulations derived from preoperative MR images of patients. The accuracy of the model was

dependent on the accuracy of these simulations, which in turn were based on assumptions about the material properties and loading conditions of the tissue. Figure 2.18 shows the process of the prediction of the final deformed point cloud using modified PointNet. While the deep neural network model provides an efficient alternative to FE simulations for real-time tasks, it still relies on FE simulations for training. This means the accuracy and reliability of the network might still be dependent on the quality and validity of these simulations.

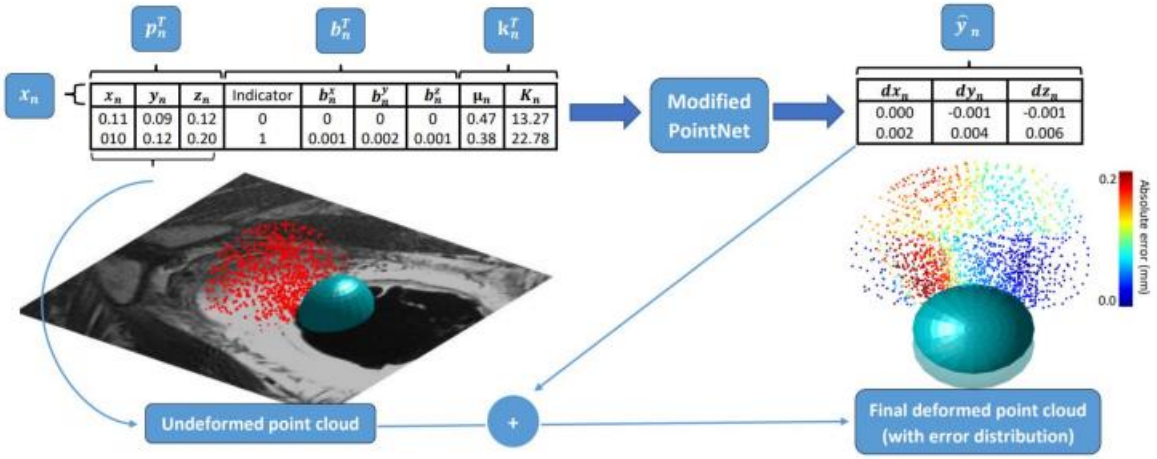

Figure 2.18 Overview of methodology of final deformed point cloud

A deep learning framework, called bidirectional point-to-point convolutional network (P2P-Conv), for orthognathic surgical planning was implemented in [46]. This framework was designed to predict subject-specific transformations between facial and bony shapes. The P2P-Conv model incorporated point-wise convolution to capture spatial information from local to global levels. The coherent point drift (CPD) algorithm was used for non-rigid registration, generating surface meshes from predicted point sets. Although, the method used surface mesh templates to reconstruct facial and bony surfaces from predicted point sets. This approach has limitations in accurately recovering shapes, as highlighted by the discrepancies between reconstructed facial surfaces and their ground truth in some examples. Also, there were some inaccuracies in the surface reconstruction due to the non-rigid registration method which may not effectively recover local shape information.

Odot *et al.* in [44] presented a novel machine learning framework to rapidly and accurately compute complex nonlinear static deformations of elastic structures. Utilizing modal analysis, a physics-

informed loss function, and an optional Hybrid Newton-Raphson algorithm, the framework demonstrated the capability to train a neural network on a limited dataset. Micrometer-scale error predictions in under a millisecond was achieved. However, the network is not able to perform well with very localized external forces and lacks inherent knowledge of topology, geometry, and Dirichlet boundary conditions. While the current model uses a fully connected network for simplicity, architectures like convolutional neural networks to enhance generalization and efficiency could be explored.

Mendizabal *et al.* [47] implemented a deep learning framework designed to model the deformable behavior of the breast during ultrasound-guided biopsies. Recognizing the computational challenges of real-time finite element method (FEM) applications, the researchers utilized a deep neural network to learn breast deformations from FEM-based simulations. Figure 2.19 depicts the samples of deformation, mean norm error and the U-Net prediction on phantom data respectively. However, a significant drawback is the time-consuming training process, which requires adaptation for every new application or geometry.

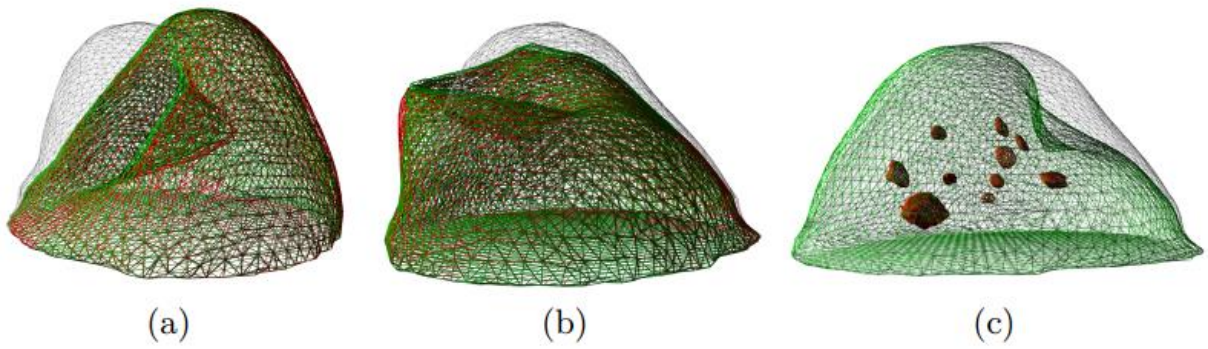

Figure 2.19 (a) Sample with maximal deformation. (b) Sample with maximal mean norm error. The green mesh is the U-Net prediction and the red mesh is the FEM solution. The initial rest shape is shown in grey. (c) U-Net prediction on phantom data.

A deep neural network strategy which merged the finite element method with U-Net architecture, was demonstrated by Brunet *et al.* [48]. It was introduced to accurately predict intricate elastic deformations during hepatic surgery for augmented reality applications. This novel approach leverages physically-based simulations of preoperative organ segmentation. Figure 2.20 shows pipeline for providing an augmented view of an organ during surgery. The network utilized a regular sparse grid input which is a feature that is achieved through an efficient FE immersed-

boundary method. However, the study primarily relied on synthetic deformations and ex vivo data, which might not encompass all complexities encountered in live surgical scenarios. Moreover, the network's dependency on a regular sparse grid input could have some challenges in diverse surgical settings.

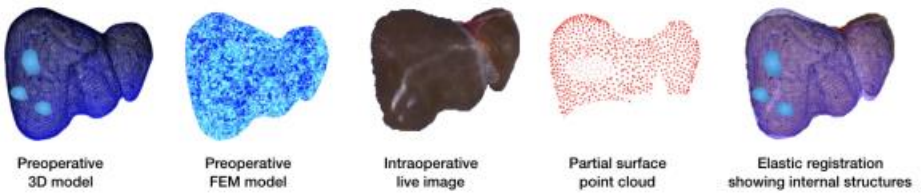

Figure 2.20 Pipeline showing preoperative internal structures are mapped in real-time onto the live image of the organ using a FEM model.

Sanchez-Gonzalez *et al.* introduced the Graph Network-based Simulators (GNS) in [49], a machine learning framework designed to simulate complex systems involving fluids, rigid bodies, and deformable materials. Utilizing particle-based representations and learned message-passing on graphs, GNS demonstrated enhanced accuracy and generalization capabilities compared to previous methods. However, some of the potential limitations include its optimization primarily for forward prediction and challenges related to parameterization and computational efficiency.

Yaman *et al.* presented a self-supervised learning method in [50] for physics-based Deep Learning MRI reconstruction when fully-sampled data is hard to procure due to constraints like organ motion and signal decay. By splitting sub-sampled points from each scan into two distinct sets, one for data consistency and the other for loss definition, the technique achieves a performance similar to its supervised counterparts, as demonstrated on the fastMRI dataset. However, the entire self-supervised approach heavily relies on available sub-sampled measurements. This reliance might be a bottleneck in scenarios where even sub-sampled data is limited or isn't of high quality.

The DLFEA (Deep Learning-based Finite Element Analysis) framework, as presented by Aditya Balu *et al.* in [51], leverages deep learning to predict aortic valve deformations. This addressed a gap in biomechanics research where previous efforts have aimed to merge physics with Deep Learning, focusing on maintaining physics consistency, integrating partial differential equations,

and distinguishing between generative and distinctive predictions. This study effectively used DLFEA to capture intricate valve interactions and deformations. Figure 2.21 shows the visualizations of the predicted and simulated deformed geometry of the leaflets and the strains computed using the simulated and predicted deformations. However, the model overlooks the anisotropy of valve tissue material. It also requires extensive patient data for customization, further validation of the Bioprosthetic heart valves (BHV) design space, and improved methods to handle out-of-distribution samples during inference.

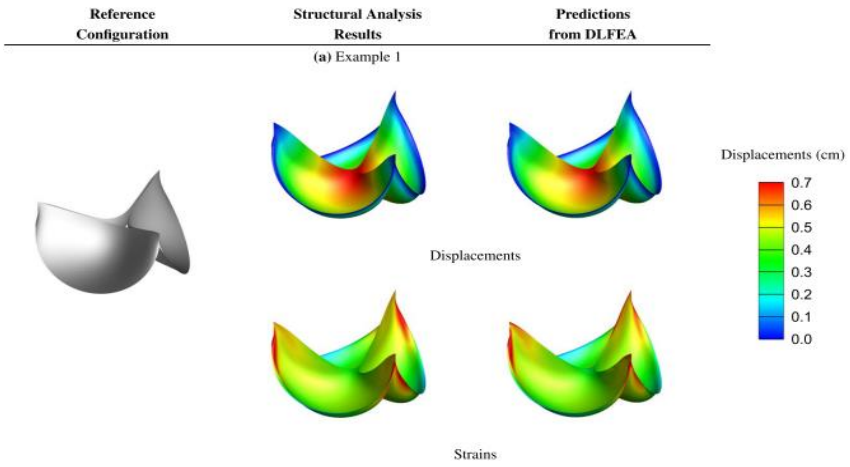

Figure 2.21 Example of valve deformations and the computed strain along with the predicted deformation using the DLFEA framework

Many of the deep learning models proposed for surgical planning and simulation, like those by Lampen *et al.* and Brunet *et al.*, specifically leverage the PointNet++ architecture or are designed for intricate simulations involving facial or hepatic deformations. For instance, in the model by Lampen *et al.*, FEM can be computationally intensive, especially for intricate structures like the human trunk in our work. When integrated into a deep learning model, this complexity can grow, potentially making real-time applications or fast simulations challenging. Sanchez-Gonzalez *et al.'s* Graph Network-based Simulators (GNS) are proficient for complex systems like fluids and deformable materials but might not be optimal for forward predictions, posing potential issues with efficiency when applied to trunk deformations. Yaman *et al.'s* self-supervised learning method, though innovative, heavily depends on sub-sampled measurements. Given the intricacies of trunk deformation, a reliance on sub-sampled data might hinder model performance, especially if such data is limited or lacks quality.

2.7 Deep Learning on 3D Point Clouds

2.7.1 PointNet

Point clouds, due to their lack of structure and non-uniform spatial distribution, are not well-suited to conventional deep learning models designed for structured data representations. To address this, a new category of models known as point-based MLP methods, pioneered by PointNet, have been developed specifically for point clouds. These models accommodate the unique properties of point clouds by not relying on any structure in the input data.

PointNet is a set function approximation model that operates on unordered collections of data, such as point clouds, making it inherently invariant to permutations in the input data. It directly processes the point cloud and extracts a set of per-point features through multiple layers of Multi-Layer Perceptrons (MLPs). These features are then processed through a symmetric function, typically max pooling, to select the most informative points. This process results in a set of global features that capture the overall characteristics of the point cloud (see Figure 2.22). The symmetry of the aggregating function ensures that the model remains invariant to the order of the input points.

For classification tasks, these global features are passed through additional MLP layers to determine class labels. For segmentation tasks, the global features are combined with the per-point features and processed through MLPs to generate a new set of per-point features that encapsulate both local geometric details and global context.

Furthermore, PointNet is designed to be invariant to rigid transformations. It employs a joint alignment network (T-Net) to predict an affine transformation, which is then applied to both the input points and the extracted per-point features at subsequent layers (see Figure 2.22). This ensures that the model's predictions are consistent regardless of the orientation or position of the input point cloud [52].

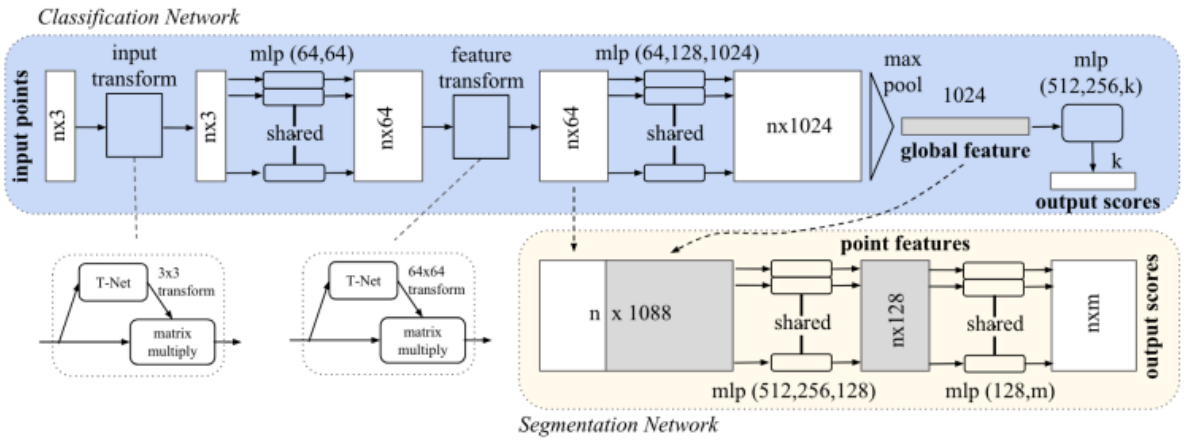

Figure 2.22 Architecture of PointNet [52]

PointNet introduced a deep learning for set functions with its innovative design, surpassing previous models in numerous 3D benchmarks. Yet, it does not leverage the local geometric structures defined by the relative distances of points in a metric space. Point clouds possess meaningful local neighborhoods based on the geometric proximity of points. By ignoring this crucial information, PointNet falls short in capturing the finer details and structures present in the input point clouds.

2.7.2 PointNet++

To overcome the limitation of PointNet, Qi et al. introduced a hierarchical feature learning approach built upon PointNet, known as PointNet++ [53]. This model is structured from multiple levels of set abstraction, each including different layers: a sampling layer, a grouping layer, and a PointNet layer. The sampling layer uses the farthest point sampling (FPS) technique to select a subset of points. The grouping layer then takes these points and positions them into local regions that overlap with one another. The PointNet module is then applied to points in each region to extract local features of the neighborhoods. This hierarchical process is repeated through several set abstraction layers, usually two to three, as illustrated in the PointNet++ original paper. This approach efficiently captures complex features (refer to Figure 2.23).

For classification, the resulting feature vectors from the topmost abstraction layer are sent through an another PointNet layer. This step helps in extracting global feature vectors. On the other hand, for segmentation tasks, the model utilizes feature propagation layers which act as the inverse of the set abstraction layers. These layers are based on point interpolation that propagate local features to their closest points. Through residual connections, these features are then integrated with the corresponding ones from previous abstraction layers. This process is repeated until per-point features for the entire set of original points are acquired. Finally, a single PointNet layer consisting of a multi-layer perceptron (MLP) is utilized to compute the final segmentation scores. By leveraging PointNet within a hierarchical framework and utilizing the inherent structure of points in a metric space, PointNet++ surpassed the performance of PointNet on 3D benchmarks and achieved state-of-the-art results at the time of its release.

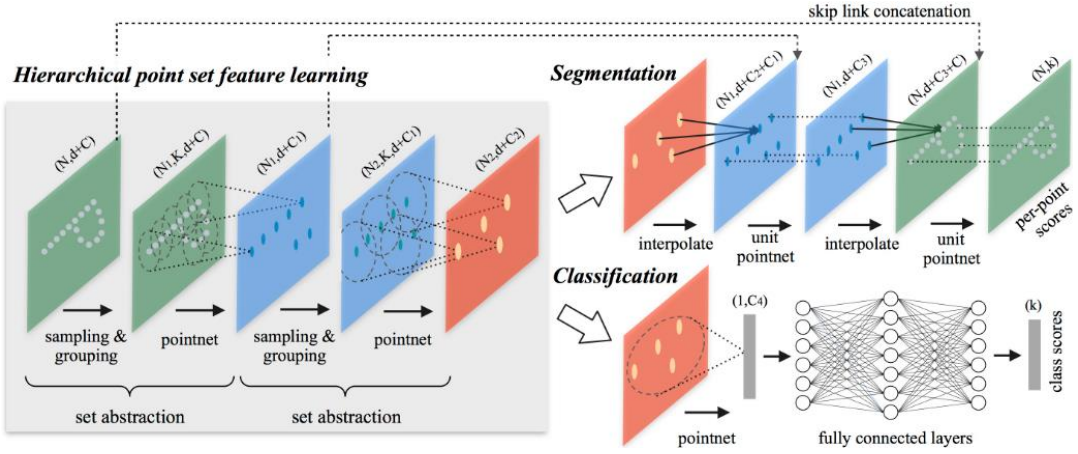

Figure 2.23 Architecture of PointNet++ [53]

2.8 Discussion

In the above sections, we have reviewed various approaches to assessing the outcome of scoliosis surgery and simulating the postoperative trunk and spine shapes. While significant advancements have been made, there remains a gap in accurately predicting the external appearance of the trunk post-surgery. The reviewed studies highlight the importance of accurate simulation and prediction models, yet few have focused specifically on the external trunk shape, which is crucial for patient satisfaction and functional outcomes.

The choice of PointNet++ as the backbone of our proposed model is motivated by its robust performance in processing point cloud data, as demonstrated in various studies. PointNet++'s hierarchical structure enables the capture of both local and global features, making it particularly suited for the complex geometry of the human trunk.

Our methodology aims to address the limitations of current approaches by providing a comprehensive framework that not only predicts the postoperative shape of the trunk but also allows for the quantitative validation of the predictions using clinical indices. By leveraging the Full Body Surface Topography (FBST) dataset and the advanced capabilities of the PointNet++ network, our method offers a promising solution to the challenges of predicting postoperative trunk shape in scoliosis patients.

In conclusion, the proposed methodology has a potential to fill a critical gap in the field of scoliosis surgery planning and evaluation. By providing a comprehensive prediction of the postoperative trunk shape, our model holds the promise of improving surgical outcomes and patient satisfaction.

2.9 Objectives

The specific objectives of this project that we aim to achieve are as follows:

- To design a deep learning architecture model to predict the postoperative shape of the trunk.
- To perform an ablation study to validate the performance of the learning model.
- To extract clinical indices from the predicted postoperative shape of the trunk
- To validate the predicted postoperative trunk shape quantitatively.

The predictions will be quantitatively validated if the model will achieve mean absolute errors within the range of 1.20° to 2.05° for Back Surface Rotation (BSR) and 1.40° to 2.20° for Trunk Rotation (TR). Furthermore, for Coronal Trunk Deviation and Sagittal Trunk Deviation, the errors are expected to range from 2.9 mm to 6 mm and 2.5 mm to 5.5 mm, respectively. These benchmarks are based on typical error measurements reported in [29], providing a basis for validating the predictive accuracy of the model.

CHAPTER 3 METHODOLOGY

The methodology for predicting the postoperative trunk shape using the proposed Deep Learning network is outlined across several sections: Section 3.1 introduces the workflow. Section 3.2 details preprocessing steps. Section 3.3 describes the model architecture. Section 3.4 discusses about the loss function. Lastly, Section 3.5 focuses on validation.

3.1 Workflow of the Proposed Method

The workflow of the proposed method is demonstrated in Figure 3.1.

The methodology for predicting the postoperative shape of the trunk using the proposed Deep Learning network is outlined in the following sections, each addressing a critical aspect of the process. The workflow and data acquisition strategy, emphasizing the importance of capturing high-quality Full Body Surface Topography (FBST) data, which serves as the foundation for accurate model predictions is presented in section 3.1. The preprocessing steps, including downsampling and normalization, which are essential for optimizing the point cloud data for effective processing by the deep learning model is delved into in section 3.2. In Section 3.3, the architecture of the proposed model is discussed, highlighting its suitability for handling point cloud data and its ability to extract both local and global features of the trunk's shape, which is crucial for accurate shape prediction. The loss function, comprising shape loss, point-density loss, and smoothness loss, which collectively guide the training process to ensure that the model learns to predict displacement vectors that accurately transform the preoperative trunk shape into the postoperative shape is discussed in section 3.4. Section 3.5 covers the validation process, which is critical for evaluating the accuracy and reliability of the model's predictions. The use of Chamfer distance as a geometric metric and clinical indices for quantitative validation ensures a comprehensive assessment of the model's performance. Lastly, the process where the trained network predicts displacement vectors for new preoperative point clouds is highlighted, and these vectors are then applied to the preoperative point cloud to generate a predicted postoperative point cloud that closely resembles the expected shape changes following the operation.

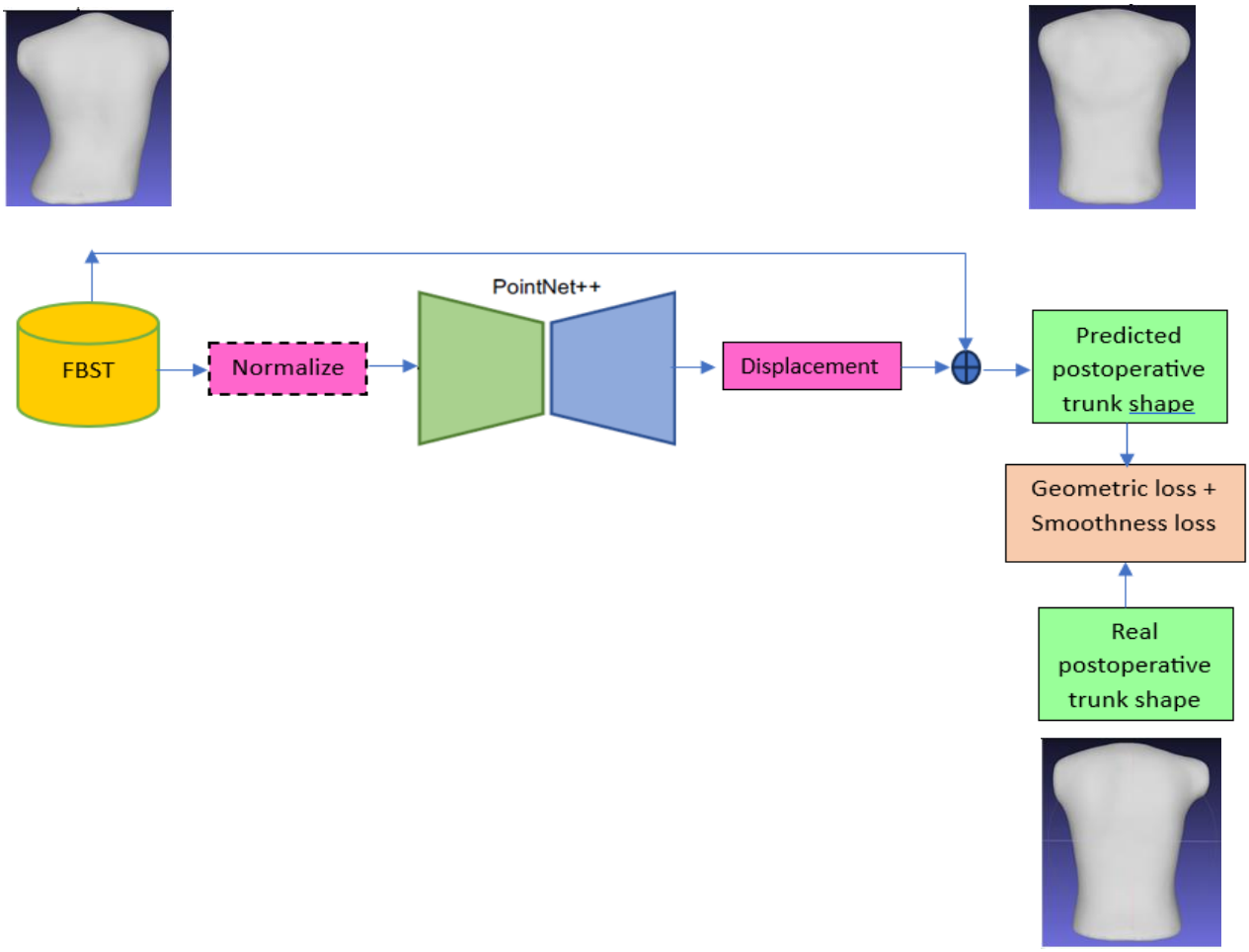

Figure 3.1 Workflow of the proposed method

The detailed implementation procedure for each of the steps are explained in the following sections.

3.1.1 Acquisition Process and Data Preparation

The proposed method uses a Full Body Surface Topography (FBST) imaging system. For obtaining FBST, the InSpeck system is used.

A dataset was created consisting of 158 patients of preoperative and postoperative trunk shape. The trunk's surface geometry is captured using a system comprising four optical 3D digitizers from Creaform Inc. Figure 3.2 shows the Raw surface mesh data obtained from InSpeck with Preoperative trunk shape and Postoperative trunk shape correspondingly.

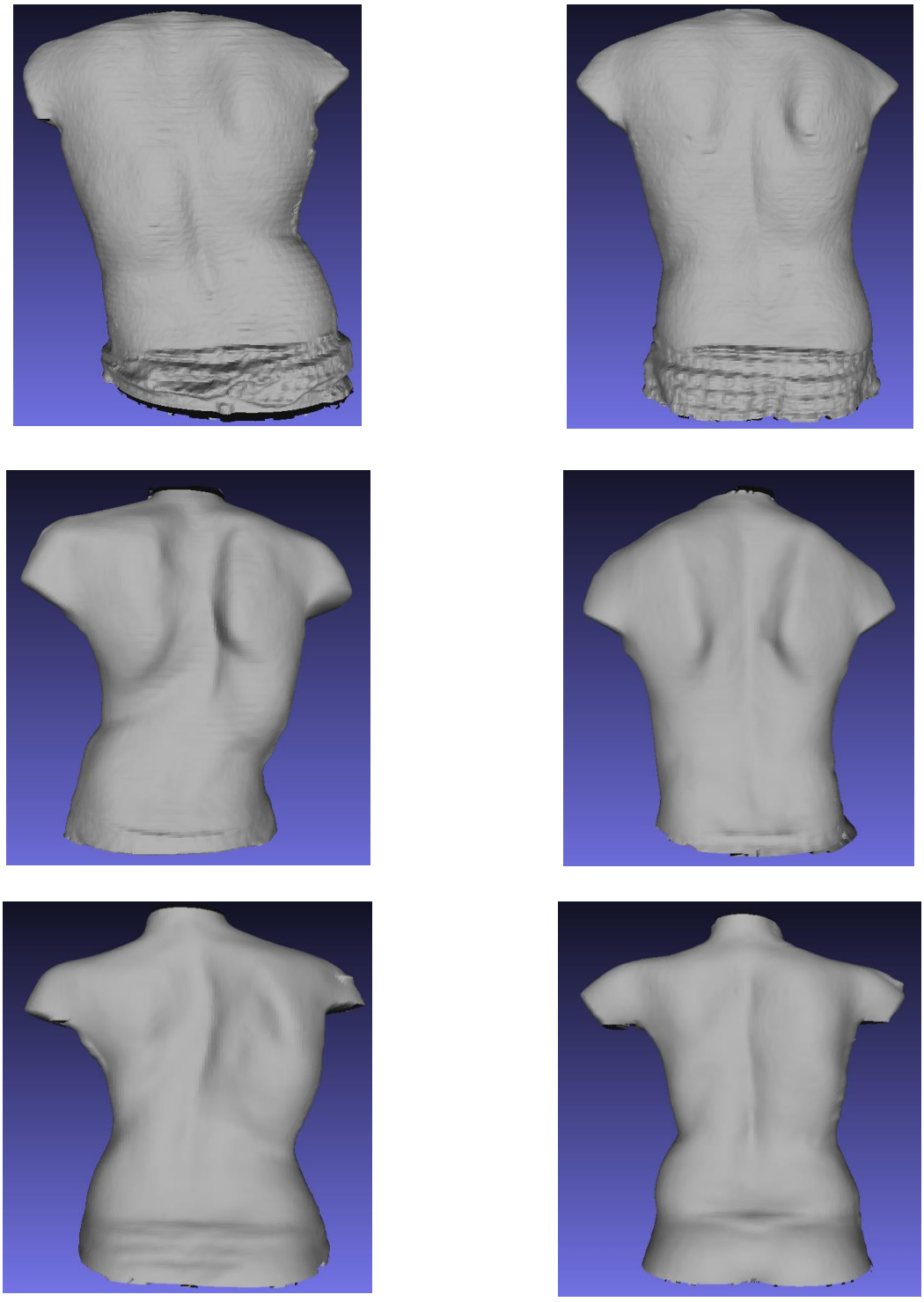

(a) (b)

Figure 3.2 Raw InSpeck Data without texture (Skin Surface) (a) Preoperative Trunk shape (b) Postoperative Trunk Shape

3.2 Preprocessing Steps

Converting (.sze) files from InSpeck to (.obj) format

The raw external trunk shape data obtained from InSpeck in the (.sze) format is converted to (.obj) file format using MeshLab. MeshLab is a powerful open-source tool used for processing and editing unstructured 3D meshes and is capable of converting various file formats, like (.sze), into more commonly used formats such as (.obj).

Smoothing trunk surface

The InSpeck system captures raw surface mesh data that may contain some noise and imperfections. To refine this data and create a smoother representation of the surface, tools like the FastRBF (Radial Basis Function) toolkit are employed. FastRBF is a tool for creating smooth interpolations from scattered data points using radial basis functions. The Fast Radial Basis Function (RBF) toolbox is used to describe scattered three-dimensional data sets with a single mathematical function. This function, known as the Radial Basis Function (RBF), is formulated as follows:

$$F(u) = q(u) + \sum_{i=1}^{N} \alpha_i \Phi \|(u - u_i)\| \tag{3.1}$$

Where $F = the\ radial\ basis\ function$

$$u = the\ surface\ point$$

$$q = low\ degree\ polynomial$$

$$\alpha_i = RBI\ coefficient$$

$$\Phi = \text{the real valued basis function}$$

$$x_i = the\ RBF\ centres$$

The basis function that was used here was **Thin-plate Spline Function** which can be represented as: $\Phi\|(u - u_i)\| = \|(u - u_i)^2 log(u - u_i)\|$. This is utilized for fitting smooth functions of two variables. It is well-suited for smooth surface interpolation where a high degree of continuity is required. This function is suitable for trunk surface smoothing because it tends to produce a very smooth surface.

The process of fitting involves finding an interpolating RBF, F_r, for a set of *N* points u_i and values g_i, such that:

$$F_r(x) = g_i \qquad for\ i = 1,2,3, \dots \dots, N \tag{4.2}$$

This fitting process allows the RBF to accurately represent the input data points and their associated values, enabling efficient interpolation of surface points in three-dimensional space. The chosen basis function influences the smoothness and characteristics of the interpolated surface [54].

Downsampling the point cloud

Here, the points in the point cloud are downsampled using uniform downsampling. The uniform downsampling of a point cloud in an OBJ file format refers to placing a grid over the given area that spans the surface of the point cloud and retaining just one sample per each cell. It reduces the point cloud by ensuring that the remaining points are evenly distributed across the spatial extent of the original dataset. The result is a more uniform representation that maintains the overall structure and distribution of the original data.

Normalizing the points in Point Cloud Data

Translating the Centroid to the Origin: The first step is to calculate the centroid of the point cloud. The centroid is simply the mean of the x, y, and z coordinates of all points in the cloud. Once the centroid is calculated, it is subtracted from each point's coordinates. This translation puts the centroid at the origin (0, 0, 0), making the distribution of points centered around the origin.

Scaling to a Specified Range: After translation, the points are scaled so that they are all within a specified range from the origin. This involves finding the maximum distance from any point to the origin and then dividing all coordinates by this distance. The points are scaled so that they are all within a distance of 1 from the origin. This scaling ensures that the point cloud fits within a standard range, regardless of its original size or position in space.

3.3 Architecture of Proposed Model

Baseline Model

PointNet++ is considered as the backbone of the proposed model due to its effectiveness in processing point cloud data because of its hierarchical structure, which enables it to capture both local and global features. The PointNet++ network is mainly used for classification and segmentation tasks.

Network Design

We modify the network according to our requirement to predict the postoperative shape of the trunk. The Deep Learning model PointNet++ network takes a point cloud as its input. This point cloud represents the preoperative shape of the trunk, with each point in the cloud characterized by its unique 3D coordinates (x, y, z). Inside the network, PointNet++ layers processes this point cloud. These layers leverage the original PointNet architecture in a hierarchical manner, working on different nested partitions of the point cloud. This hierarchical application helps the network extract both localized and global features from the point cloud. Figure 3.3 PointNet++ Network Designshows the network design of PointNet++ network adapted for our purpose as follows:

i. **Input Layer (Preoperative Point Cloud):** The input to the network is a point cloud representing the preoperative shape of the trunk. Each point in the cloud is represented by the (x, y, z) 3D coordinates.

ii. **PointNet++ Layers (Sampling & Grouping, PointNet, Aggregation):** These layers apply the original PointNet in a hierarchical manner on nested partitions of the point cloud. This allows the network to capture local features from small neighborhoods of points, as well as global features from larger regions. The output of these layers is a high-dimensional feature vector for each point in the cloud.

    a. **Sampling and Grouping (SG) Layers:** In each PointNet++ layer, the point cloud is first partitioned into overlapping local regions by a sampling and grouping operation. This is done by a farthest point sampling (FPS) strategy, which selects a subset of points that are spread out over the entire cloud. Each selected point is then associated with its nearest neighbors to form a local region.

    b. **PointNet Layers:** The original PointNet [5] is applied to each local region to extract local features. This involves several shared MLPs and a max pooling operation. The

output is a feature vector for each local region, capturing the local geometric structure of the region.

c. **Aggregation Layer:** This layer aggregates the local features from all regions to obtain a global feature vector. This is done by a max pooling operation, which captures the most significant features across all regions.

iii. **Feature Propagation Layers**: After the network has encoded the point cloud features through a series of downsampling and feature extraction steps, the feature propagation layers have its role. These layers are responsible for upsampling and refining the feature vectors to match the resolution of progressively denser layers of the point cloud. This process allows the network to reconstruct detailed point-wise features that are important for making precise predictions.

a. **First Propagation Layer**: It begins the up-sampling process by propagating features from the sparsest layer to a denser layer. It considers the spatial information contained in the 3D coordinates to guide the interpolation process. The interpolated features are then processed through MLPs to enhance the feature representation.

b. **Additional Propagation Layers**: The up-sampling process is continued, increasing the density of the point cloud progressively and enhancing the features until the original resolution is reached.

iv. **Fully Connected (FC) Layers**: These layers take the up-sampled feature vectors as the input and output the displacement vectors for each point in the point cloud. The final layer uses sigmoid activation function to output the displacement vectors.

v. **Output Layer:** The output of the network is the predicted displacement vectors for each point in the cloud.

Finally, the predicted displacement vectors are applied to the original preoperative point cloud to obtain a predicted postoperative point cloud.

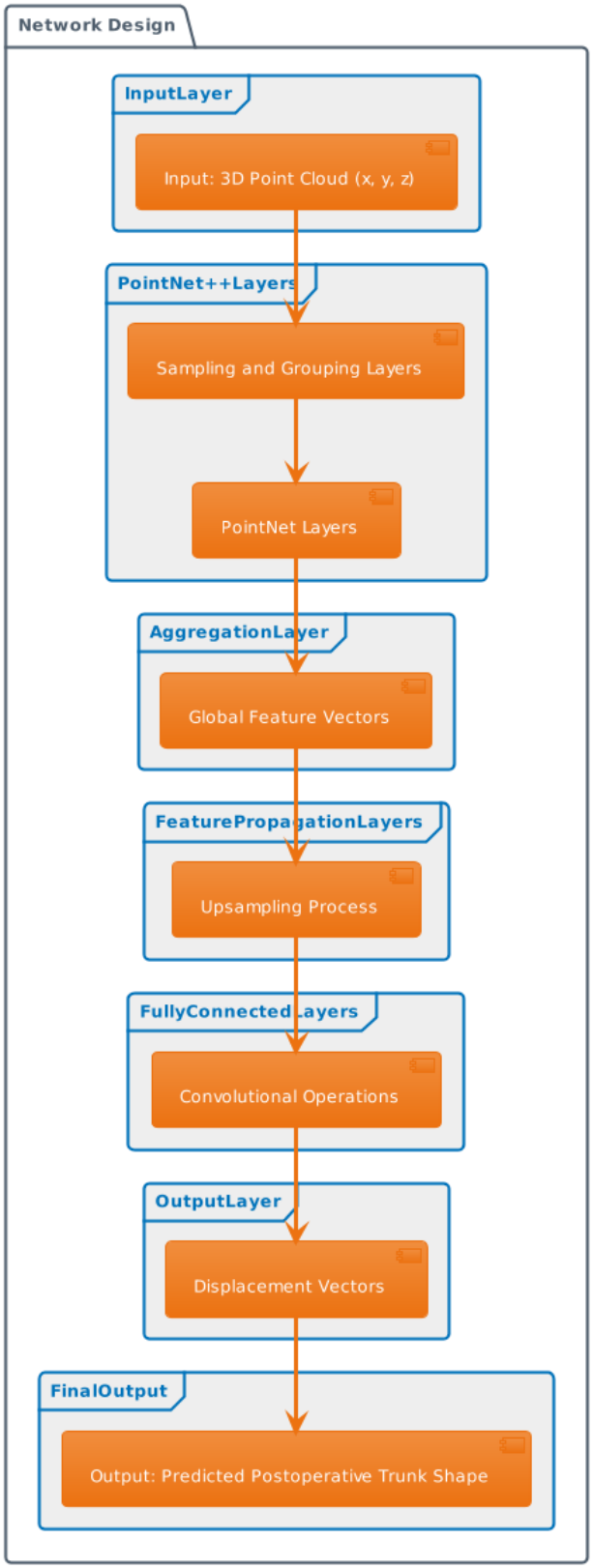

Figure 3.3 PointNet++ Network Design

3.4 Loss Function

Training encompasses learning displacements and defining the loss function. During this phase, the network learns to predict displacement vectors that transforms the preoperative shape into the postoperative shape, having a geometric loss function that accounts for shape loss, point-density loss, and smoothness loss.

1) Geometric Loss: A geometric loss L_g is used to measure the geometric differences between the predicted and target point sets. This loss consists of two terms: shape loss and point-density loss [6].

a) Shape Loss: The use of shape matching loss allows our model to ensure that the predicted postoperative trunk shape (transformed point set $\hat{P}$) is as close as possible to the actual postoperative trunk shape (target point set P). This loss function penalizes the model if the predicted shape deviates from the target shape.

Shape loss, L_{shape}, computed by summing distance errors between predicted point set, $\hat{P}$, and target point set, P.

$$L_{\text{shape}}(\hat{P}, P) = \sum_{p \in P} \min_{q \in \hat{P}} d\,(p, q) + \sum_{q \in \hat{P}} \min_{p \in P} d\,(p, q) \tag{4.2}$$

where $d\,(p, q)$ denotes the Euclidean distance between points p and q.

$L_{shape}(\hat{P}, P)$: The shape loss between the predicted point set $\hat{P}$ and the actual (target) point set P.

$\sum_{p \in P} \min_{q \in \hat{P}} d\,(p, q)$: This sum iterates over all points p in the actual point set P. For each point p in the actual point set P, this finds the point q in the predicted point set $\hat{P}$ that is closest to p and calculates the distance $d\,(p, q)$ between p and this nearest point q. The function $d\,(p, q)$ is a Euclidean distance measure.

$\sum_{q \in \hat{P}} \min_{p \in P} d\,(p, q)$: This sum iterates over all points q in the predicted point set $\hat{P}$. For each point q in the predicted point set $\hat{P}$, this finds the point p in the actual point set P that is closest to q and calculates the distance $d\,(p, q)$ between q and this nearest point p.

Combining these two sums, the shape loss is the sum of the smallest distances from each point in one set to the nearest point in the other set. This encourages the predicted point set to align closely with the actual point set by minimizing the distances between corresponding points.

b) Density Loss: The density loss term accounts for the local distribution of points. It measures the discrepancy in the density of points between the predicted point set and the target point set. In the context of predicting the postoperative trunk shape, this is essential because the distribution of points can impact the overall shape prediction. By incorporating a density loss term, our model is encouraged to match the overall shape as well as the underlying point distributions that collectively form that shape.

Density Loss, $L_{density}$, measures density similarity between $\hat{P}$ and *P.*

$$L_{density}(\hat{P}, P) = \frac{1}{k}\sum_{p\in P}\sum_{i=1}^{k}\left|d(x, O_i[P, x]) - d\left(x, O_i\left[\hat{P}, x\right]\right)\right| \tag{4.3}$$

$L_{density}(\hat{P}, P)$: The density loss between the predicted point set $\hat{P}$ and the actual (target) point set P.

$\frac{1}{k}$: k is the number of nearest neighbors considered for each point. It averages the loss over these neighbors.

$\sum_{p\in P}\sum_{i=1}^{k}\left|d(x, O_i[P, x]) - d(x, O_i\left[\hat{P}, x\right])\right|$: This sum iterates over all points p in the actual point set P. This inner sum iterates over the k nearest neighbors. This term calculates the absolute difference between two distances:

$d(x, O_i[P, x])$: The distance between the point x and its i-th nearest neighbor in the actual point set P.

$d(x, O_i\left[\hat{P}, x\right])$: The distance between the point x and its i-th nearest neighbor in the predicted point set $\hat{P}$.

The density loss measures how well the local point density around each point x in the actual point set P is replicated in the predicted point set $\hat{P}$. By considering the distances to the k nearest neighbors, the loss considers the local distribution of points around each point.

The geometric loss L_g can be defined as:

$$L_g(\hat{P}, P) = \alpha L_{shape}(\hat{P}, P) + \beta L_{density}(\hat{P}, P) \tag{4.4}$$

$L_g(\hat{P}, P)$: This represents the total geometric loss function between the predicted point cloud ($\hat{P}$) and the ground truth point cloud (P). The goal is to minimize this value during training, which means that the predicted point cloud is becoming more similar to the ground truth.

α : This is a weighting factor for the shape loss component of the total loss. By adjusting α, we can control the importance of the shape loss relative to the density loss in the total loss function.

$L_{shape}(\hat{P}, P)$: This is the shape loss component. It measures how well the predicted point cloud ($\hat{P}$) matches the shape of the ground truth point cloud *(P)*.

β : Similar to α, β is a weighting factor for the density loss component. It balances the influence of density loss in the calculation of total loss.

$L_{density}(\hat{P}, P)$: This is the density loss component, which calculates the similarity in point distribution or density between the predicted point cloud ($\hat{P}$) and the ground truth point cloud (P).

2) Smoothness Loss

Along with this geometric loss function, we also consider a smoothness loss function to deal with the smoothness of the displacements. This function ensures that the predicted displacements are smooth by penalizing large differences in the displacements of neighboring points. Since we are dealing with point clouds representing the shape of the trunk, we assume that the displacement of points in the point cloud should generally be smooth - i.e., neighboring points should have similar displacements.

The smoothness loss can be defined as:

$$L_{smooth} = \sum_{i=1}^{N} \left(\frac{1}{|\mathcal{N}_i|} \sum_{j \in \mathcal{N}_i} \left\| u(x_i) - u(x_j) \right\|^2 \right) \tag{4.5}$$

L_{smooth}: The smoothness loss for the entire point cloud or mesh.

$\mathcal{N}_i$: The set of neighboring points for the i-th point.

$|\mathcal{N}_i|$: The cardinality of this set which gives the number of neighbors.

$u(x_i)$: The displacement of the *i*-th point.

$u(x_j)$: The displacement of the *j*-th point, which is a neighbor of the *i*-th point.

$\left\|u(x_i) - u(x_j)\right\|^2$: The squared Euclidean distance between the displacement vectors of the *i*-th point and its *j*-th neighbor. This measures how much the displacement of neighboring points differs.

The expression $\frac{1}{|\mathcal{N}_i|}\sum_{j\in\mathcal{N}_i}\left\|u(x_i) - u(x_j)\right\|^2$ calculates the average squared difference in displacement between a point *i* and all of its neighbors. By averaging over the entire set of points *i* =1 to *N*, the model enforces a smooth transition across the whole point cloud.

The **total loss** would be a combination of the two terms:

$$Loss = L_{geo} + \gamma L_{smooth} \tag{4.6}$$

Loss is the total loss function, L_{geo} is the geometric loss, L_{smooth} is the smoothness loss, γ represents the weight for the smoothness loss.

3.5 Validation

Data Split: The dataset is divided into three parts: 70% is used for training the model, 10% is used for validation (tuning hyperparameters, preventing overfitting), and the remaining 20% is used for testing (evaluating the model's performance on unseen data).

We use Chamfer distance as quantitative validation metric to measure prediction accuracy. Chamfer Distances (CD) is used to measure shape error in predicted surfaces; a measure of nearest neighbor distances between two point clouds.

$$d_{CD}(S_1, S_2) = \frac{1}{|S_1|}\sum_{x\in S_1}\min_{y\in S_2}\|x - y\|_2^2 + \frac{1}{|S_2|}\sum_{y\in S_2}\min_{x\in S_1}\|x - y\|_2^2 \tag{4.7}$$

The Chamfer distance between the two point clouds S_1 and S_2 can be computed using the following steps:

1) For each point x in set S_1, we find the point y in set S_2 that is closest to x and calculate the squared Euclidean distance between x and y. This is computed as:

$$d_{CD}(x, S_2) = \min_{x \in S_1} \|x - y\|_2^2 \tag{4.8}$$

2) Then, we calculate the average of all the minimum squared distances obtained in step 1. This gives us the first part of the Chamfer distance, which can be represented as:

$$\frac{1}{|S_1|} \sum_{x \in S_1} \min_{y \in S_2} \|x - y\|_2^2 \tag{4.9}$$

3) Now, performing a similar operation in reverse, where for each point y in set S_2, we find the point x in set S_1 that is closest to y and compute the squared Euclidean distance. This is computed as:

$$d_{CD}(y, S_1) = \min_{x \in S_1} \|x - y\|_2^2 \tag{4.10}$$

4) Then, we calculate the average of all the minimum squared distances obtained in step 3. This gives us the second part of the Chamfer distance, represented as:

$$\frac{1}{|S_2|} \sum_{y \in S_2} \min_{x \in S_1} \|x - y\|_2^2 \tag{4.11}$$

5) The Chamfer distance $d_{CD}(S_1, S_2)$ is then the sum of the averages obtained in steps 2 and 4. This provides a measure of the overall difference between the two point sets, accounting for the nearest neighbor distances in both directions.

3.5.1 Clinical Validation

The following Clinical indices are used to compare differences between the predicted and actual trunk surface which are present in the Torso 3D application:

Figure 3.4 shows the illustration of these clinical indices [9].

1. **Back Surface Rotation (BSR):** This measures the rotation of the back surface. It measures the difference between the predicted and actual rotation angles of the trunk. A higher BSR value indicates greater asymmetry.
2. **Trunk Rotation (TR):** TR assesses the rotational deviation of the entire trunk. It considers both the frontal and sagittal planes.
3. **Coronal Trunk Deviation (CTD):** This measures the lateral deviation of the trunk in the coronal plane (the plane that divides the body into front and back). It helps to assess how much the spine deviates from an ideal vertical alignment when viewed from the front or back.
4. **Sagittal Trunk Deviation (STD):** This is the measurement of the deviation or curve of the trunk in the sagittal plane (the plane that divides the body into left and right). It evaluates the difference between the predicted and actual sagittal alignment. It assesses the forward or backward bending of the trunk, which could indicate a posture issue or a sagittal imbalance.
5. **Depth Asymmetry (DA):** This measures asymmetry in the depth of the trunk, the prominence of the ribs or shoulder blade when bending forward. It's often used to assess the rotational component of scoliosis, where one side of the rib cage may protrude more than the other [29] [55] [56].

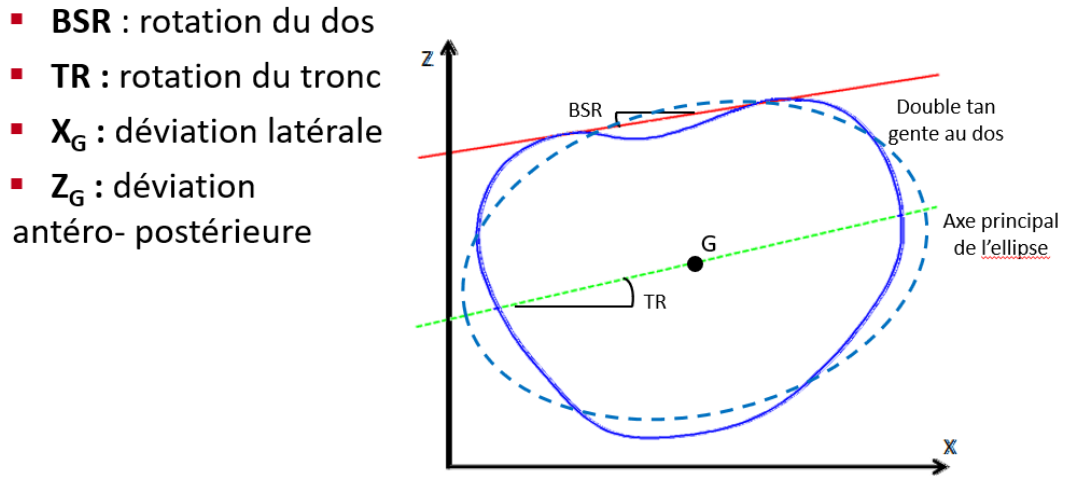

Figure 3.4 Clinical Measurements [9]

3.6 Post-Processing

After getting the postoperative point cloud, the post-processing of the point cloud is done using MeshLab. In MeshLab, first the normal for point sets is computed, then the surface of the point cloud is reconstructed using the Poisson surface reconstruction which we can see in the images in Table 4.5. Using the Poisson surface reconstruction algorithm [57], a smooth and continuous surface is created from the point cloud and its normals. This algorithm effectively fills in gaps and removes noise from the point cloud, resulting in a more accurate representation of the trunk's surface.

Poisson surface reconstruction involves the following steps:

1. **Input**: A set of oriented points$\{(p_i, n_i)\}$, where p_i is the position and n_i is the normal vector of the i-th point.
2. **Gradient Field**: Construct a vector field V such that $V \approx n_i$ at points p_i.
3. **Poisson Equation**: Formulate the problem as solving the Poisson equation $\Delta\chi = \nabla \cdot V$, where χ is the indicator function, Δ is the Laplacian operator, and $\nabla \cdot V$ is the divergence of V.
4. **Discretization**: Discretize the domain and represent χ and V on a grid or an adaptive structure like an octree.
5. **Linear System**: Convert the Poisson equation into a sparse linear system $Ax = b$, where A represents the Laplacian, x is the unknown χ, and b is the divergence of V.
6. **Solve**: Solve the linear system $Ax = b$ to obtain the values of the indicator function χ.
7. **Surface Extraction**: Extract the reconstructed surface as the isosurface of χ using algorithms like marching cubes [57].

CHAPTER 4 RESULTS AND DISCUSSION

This section of the dissertation presents and analyzes the results obtained from the modified PointNet++ architecture for predicting the postoperative shape of the trunk. It includes quantitative results, visualizations, and discussions. It details the performance of the deep learning model in accurately estimating postoperative trunk shape from preoperative point cloud data. Additionally, it outlines the values of different parameters used in the model, including the loss function components.

4.1 Dataset Distribution and Training Parameters

Our dataset comprised 158 AIS patients who underwent surgery at Sainte-Justine Hospital Center, Montreal, Canada. We used 70% of our data for training, 20% for testing and 10% for validation which means 111 patients for Training, 32 patients for Testing and 15 patients for Validation.

4.1.1 Summary Statistics of the Dataset

The statistical overview of the dataset consisting of some of the variables Age, Height, weight and BMI is given as follows in the following Table 4.1 .

Table 4.1 Statistical Overview of the data.

Variable	Mean ± STD	Range (min, max)
Age (years)	14.8 ± 2.35	(9, 21)
Height (cm)	158.5 ± 8.68	(137.2, 188.8)
Weight (kg)	52.3 ± 12.55	(29.1, 108.2)
BMI (kg/m^2)	20.71 ± 4.44	(14.73, 44.01)

Distribution of other variables:

Lenke Classification Frequency Distribution

Table 4.2 shows the Lenke Classification for each of the Curve Type.

Table 4.2 Lenke Classification Frequency Distribution

Lenke Classification	**1A**	**6C**	**5C**	**2A**	**1B**	**3C**	**1C**	**3A**	**2C**	**3B**	**2B**	**4B**	**4C**	**4A**
Count	50	22	21	19	19	17	11	10	6	6	3	3	2	2

Surgeon Frequency Distribution:

Surgeon 1: 91

Surgeon 2: 54

Surgeon 3: 33

Surgeon 4: 9

Surgeon 5: 4

4.1.2 Hyperparameters

The network was trained for 150 epochs using the Adam optimizer, a batch size of 6, a learning rate of 0.001, and a decay rate of 0.5. Also, the weights for each of the loss function α, β, γ were considered as 1. This configuration was chosen to maintain a standard approach, ensuring each component contributed equally to the model's learning without any specific tuning.

4.2 Visualization of Results and Analysis

4.2.1 Visualization of pre-processed point cloud

Table 4.3 Pre-processed point cloud

Preoperative	Ground Truth
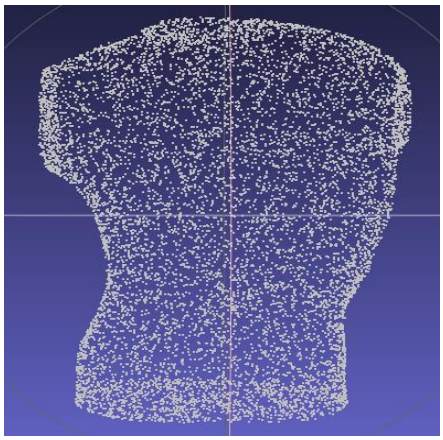	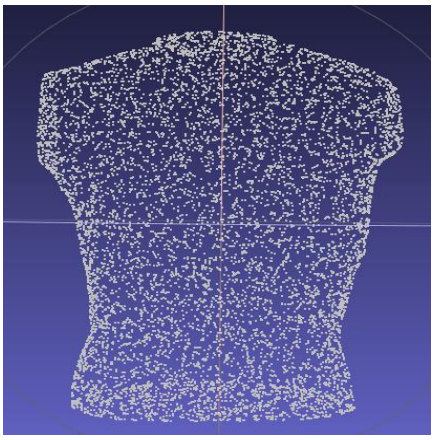
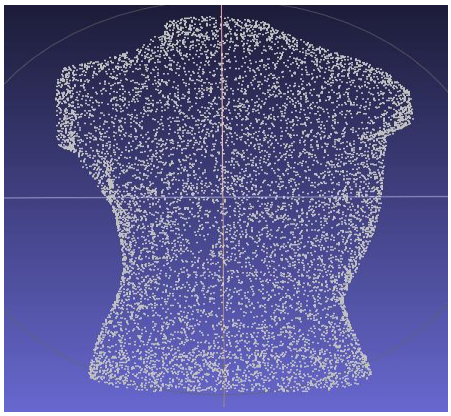	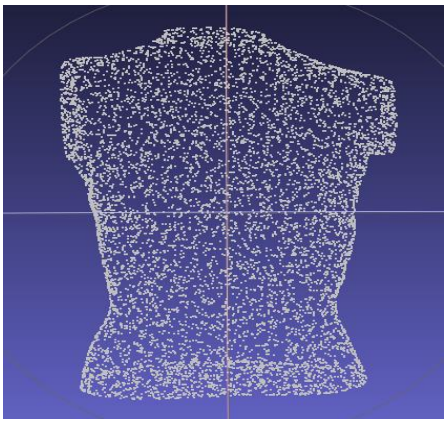
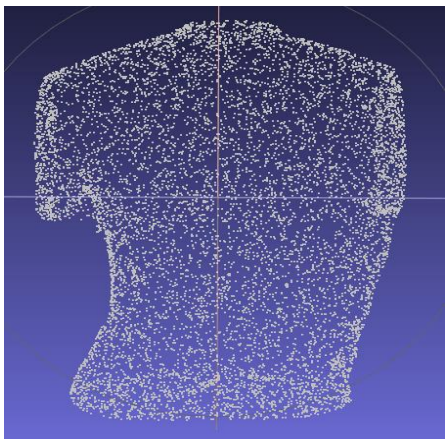	

From Table 4.3, we can see that the preprocessed point cloud can be descried as visually cleaner, more structured, and uniformly scaled representation of the original trunk shape data. The downsampling process results in a point cloud with fewer points, but these points are evenly distributed across the surface, maintaining the overall shape and structure of the trunk. The normalization step ensures that the point cloud is centered at the origin and scaled to fit within a standard range, making it more consistent and easier to work with.

4.2.2 Visualization of Predicted Results

The raw output of the PointNet++ model is a set of points in a point cloud that represent the predicted postoperative shape of the trunk which is shown in Table 4.4. However, for visualization, analysis, and further processing, it is necessary to reconstruct a continuous surface from these discrete points. MeshLab provides algorithm like Poisson surface reconstruction to create a continuous surface mesh from the point cloud which we already discussed in section 3.6.

For Poisson Surface Reconstruction in the MeshLab, the parameter of Number of Neighbors is set as 750 for computing the normals for point sets. It determines the number of nearby points used to estimate the normal at each point.

Table 4.4 Predicted Results obtained from the network

Preoperative	Predicted Postoperative	Ground Truth
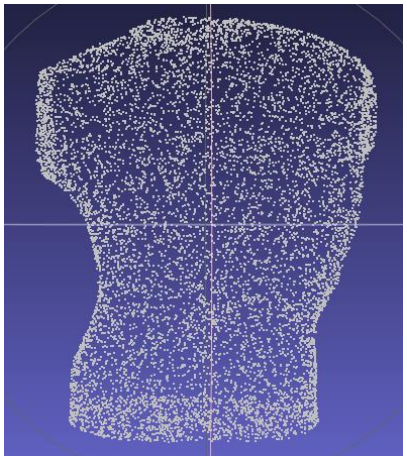	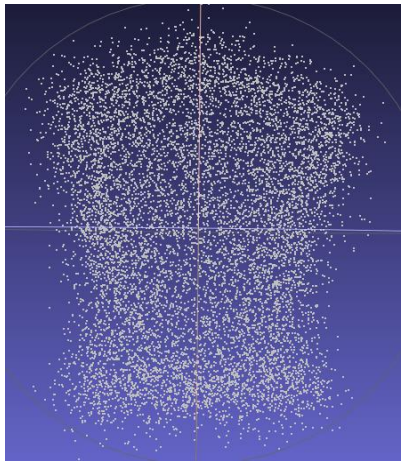	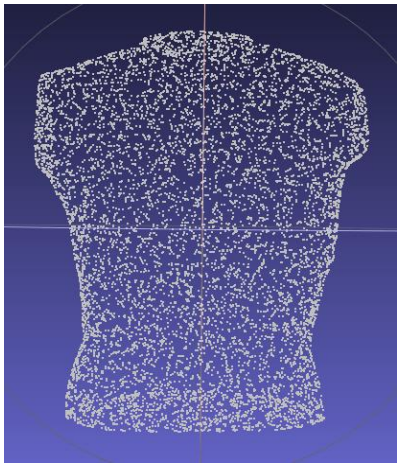
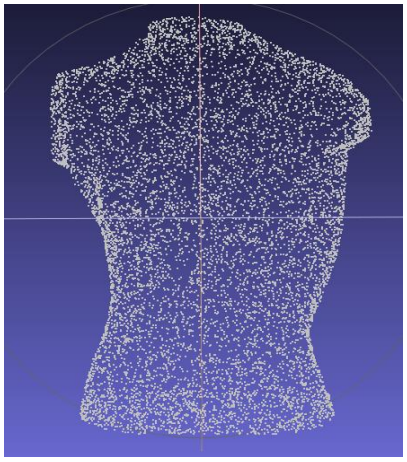	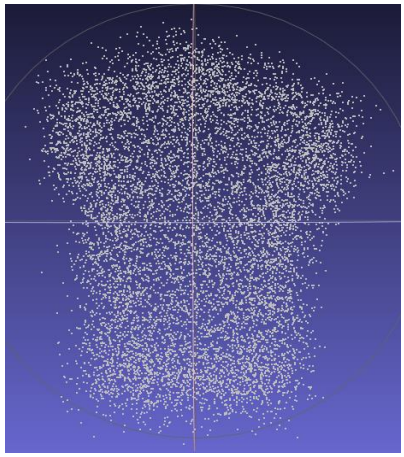	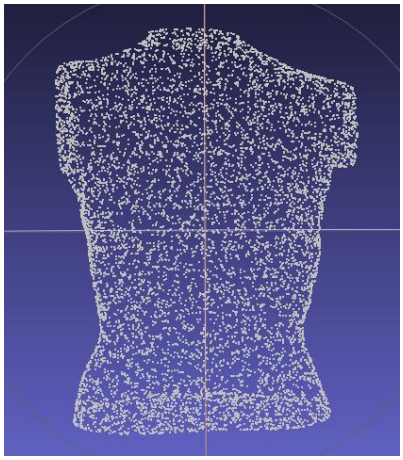
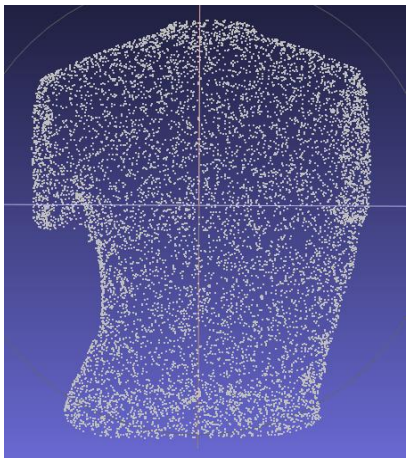	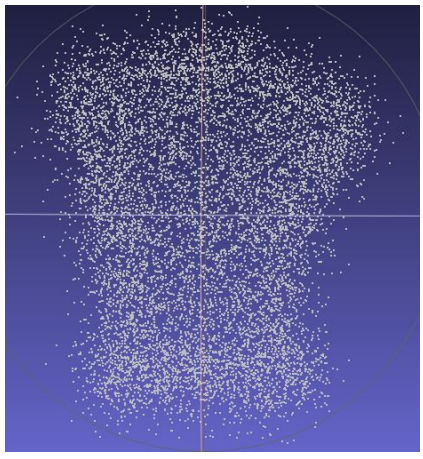	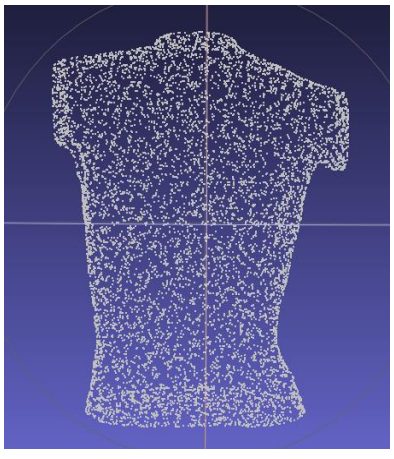

Table 4.5 Visualization of Results after Post-processing

Preoperative	Predicted Postoperative	Ground Truth
		
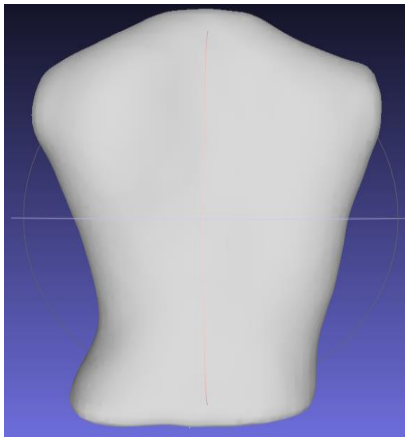	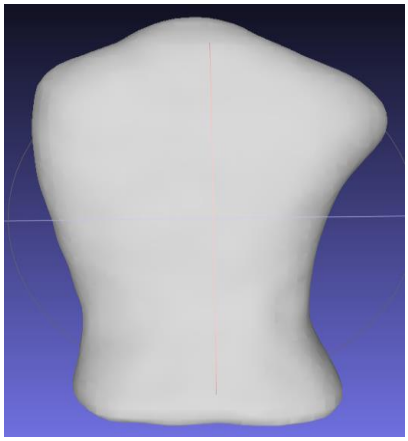	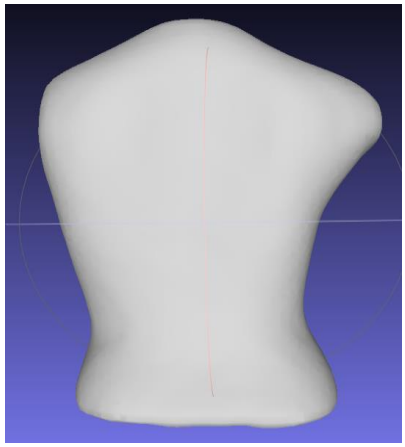
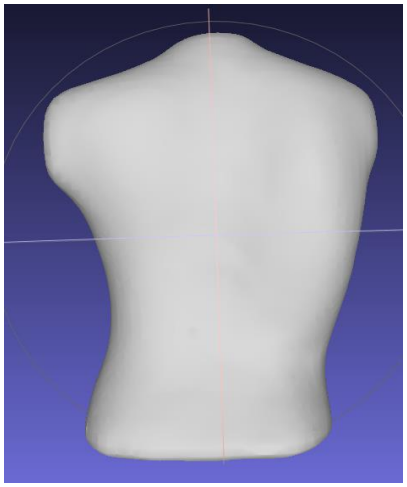	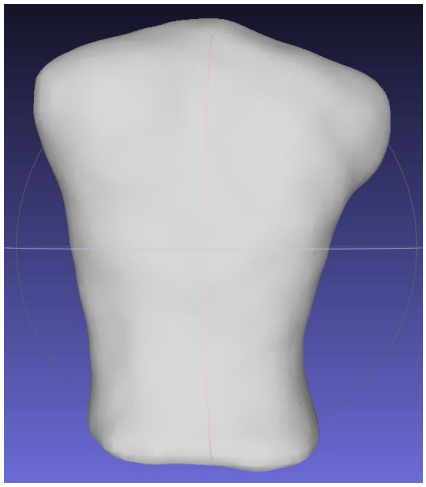	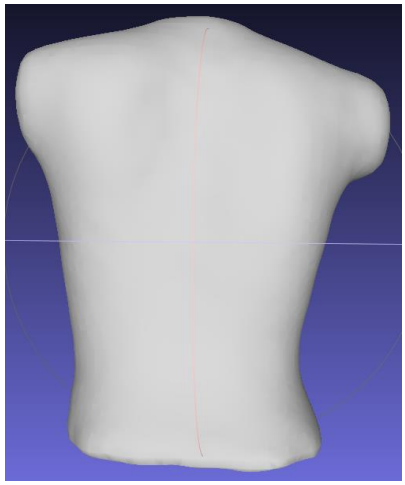

4.3 Ablation Study

This section explores the impact of the different loss function components that we used on the performance of our deep learning model. We focus on the geometric loss (encompassing shape loss and density loss) and the smoothness loss. By systematically evaluating different combinations of these losses, we aim to understand their individual and collective contributions to model accuracy and generalization as shown in Table 4.6.

Table 4.6 Ablation Study Experiments

Experiment No.	Geometric Loss		Smoothness Loss
	Shape Loss	Density Loss	
1 (Baseline-All Losses)	✓	✓	✓
2	✓	✓	
3	✓		✓
4		✓	✓

4.3.1 Experiment 1 (Considering all loss)

Experiment 1 (Considering all loss) evaluates the performance of the deep learning model when all components of the loss function are included. This experiment serves as a baseline to assess how well the model can predict the postoperative trunk shape when shape loss, density loss, and smoothness loss are all incorporated. By including all loss components, the model is expected to capture both the overall shape and the detailed geometrical features of the trunk, as well as ensure smooth transitions between neighboring points.

Considering both components of geometric loss (shape and density) and smoothness loss, we have analysed and presented the results by a visual comparison of predicted vs. actual trunk shapes in Table 4.5 along with clinical indices analysis derived from the predicted postoperative trunk shapes. It showcases the effectiveness of the combined loss function in accurately predicting the postoperative trunk shape.

4.3.2 Experiment 2 (Considering Geometric Loss (Shape loss + Density Loss) and *without* Smoothness Loss)

Experiment 2 (Considering Geometric Loss (Shape loss + Density Loss) and without Smoothness Loss) is conducted to assess the impact of excluding smoothness loss on the performance of the model. By focusing only on geometric loss, which includes shape loss and density loss, this experiment aims to understand how well the model can predict the postoperative trunk shape when smooth transitions between neighboring points are not enforced.

4.3.3 Experiment 3 (Considering Shape Loss, Smoothness Loss and *without* Density Loss)

Experiment 3 (Considering Shape loss, Smoothness Loss, and without Density Loss) evaluates the model's performance when density loss is excluded from the loss function. By focusing on shape loss and smoothness loss, this experiment aims to understand the significance of maintaining point density uniformity in the predicted postoperative trunk shape. The exclusion of density loss allows us to assess the model's ability to accurately capture the overall shape and smooth transitions between neighboring points while potentially forgoing uniformity in point distribution.

4.3.4 Experiment 4 (Considering Density Loss, Smoothness Loss and *without* Shape Loss)

Experiment 4 (Considering Density Loss, Smoothness Loss, and without Shape Loss) is designed to assess the model's performance when shape loss is excluded from the loss function. By focusing on density loss and smoothness loss, this experiment aims to understand the impact of excluding shape accuracy from the model. The exclusion of shape loss allows us to evaluate the model's ability to maintain uniform point distribution and smooth transitions between points while compromising the accuracy of the overall shape.

Experiment 2: Considering Geometric Loss (Shape loss + Density Loss) and *without* Smoothness Loss

Table 4.7 Experiment 2 Visualization Results

Ground Truth	With Geometric Loss (Shape Loss + Density Loss) and *without* Smoothness Loss
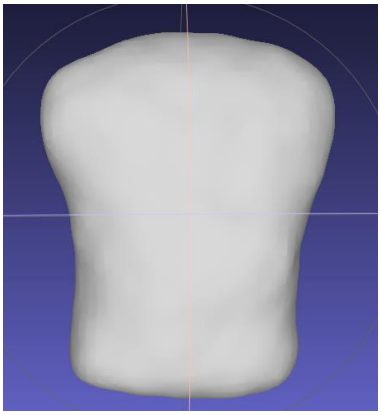	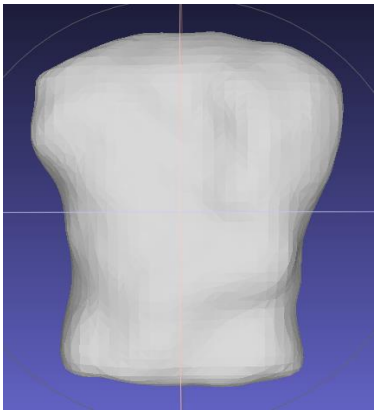
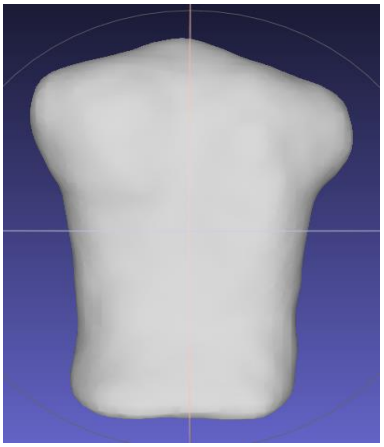	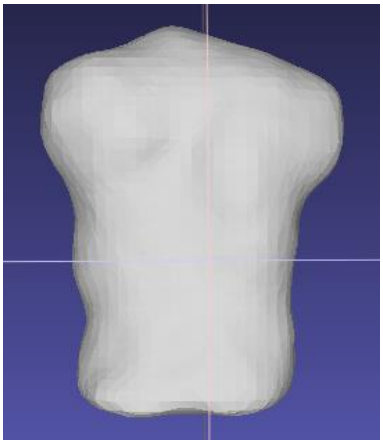
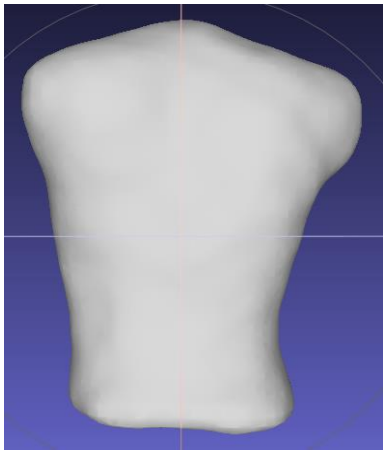	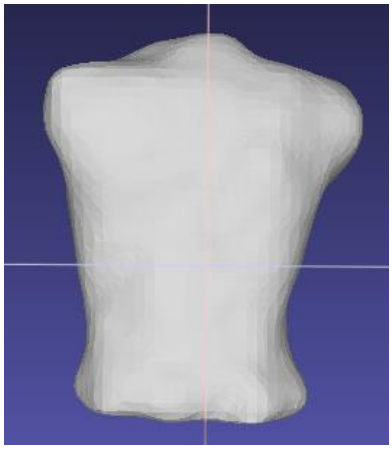

Experiment 3: Considering Shape Loss, Smoothness Loss and *without* Density Loss

Table 4.8 Experiment 3 Visualization Results

Ground Truth	**With Shape Loss, Smoothness Loss and *without* Density Loss**
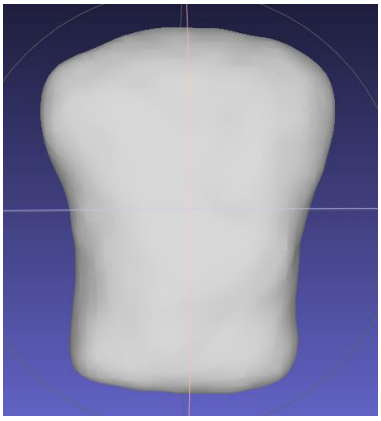	
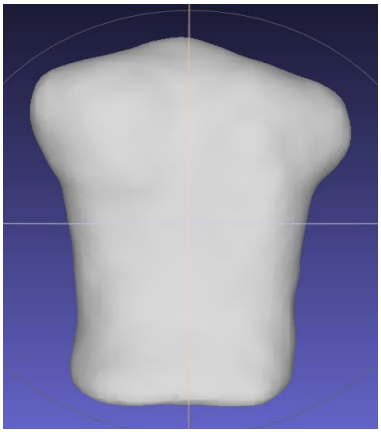	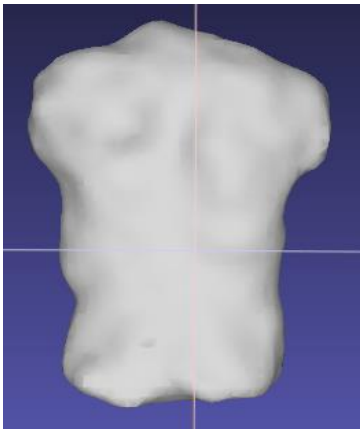
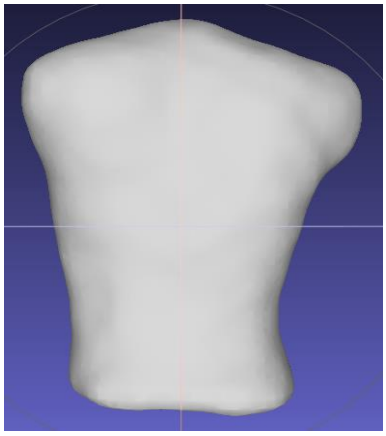	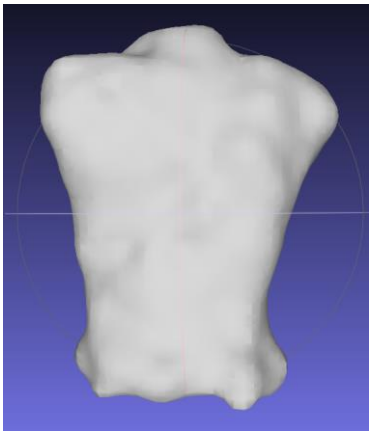

Experiment 4: Considering Density Loss, Smoothness Loss and without Shape Loss

Table 4.9 Experiment 4 Visualization Results

Ground Truth	**With Density Loss, Smoothness Loss and *without* Shape Loss**
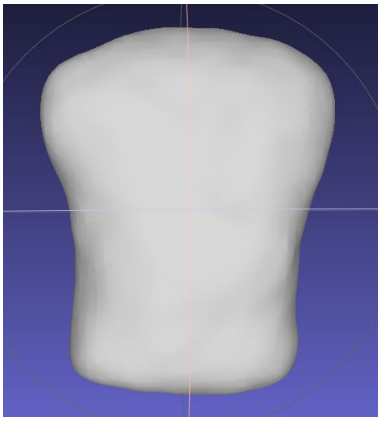	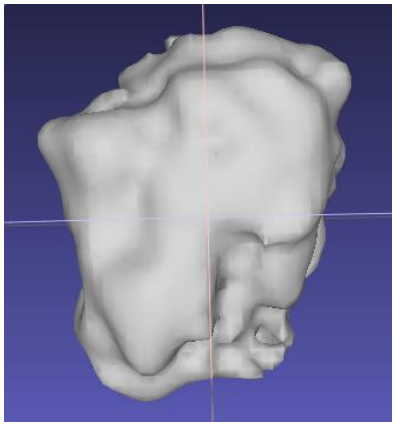
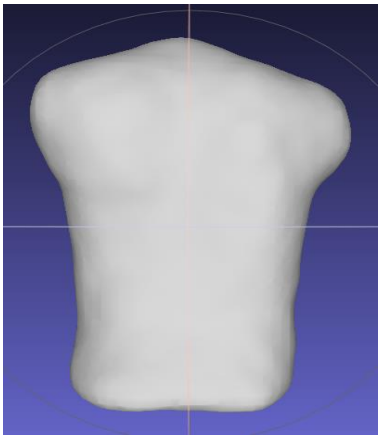	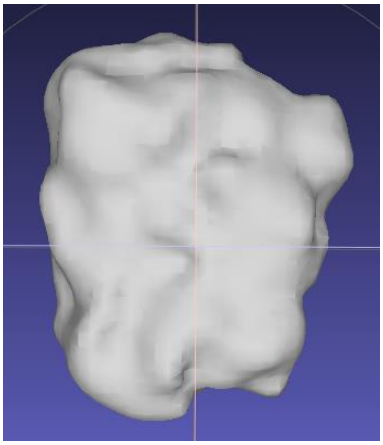
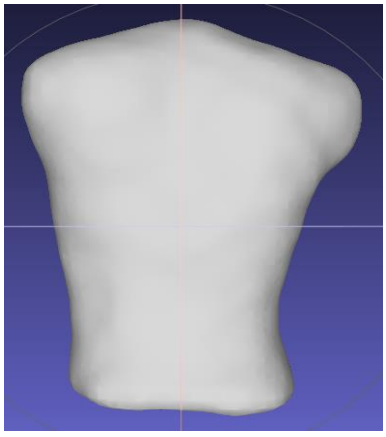	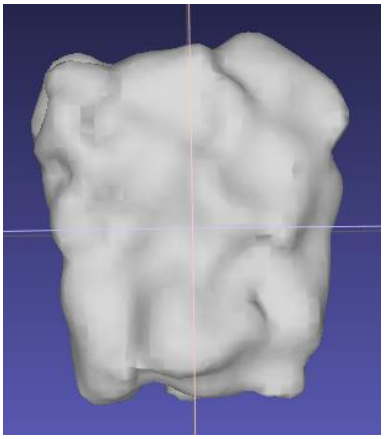

For Experiment 2 (without Smoothness Loss):

From the visualizations of Table 4.10, we can notice that the surface of the trunk appears rough. The surface lacks the continuity and smooth transitions that are characteristic of natural trunk surfaces, without the smoothness loss to penalize large variations in displacement between neighboring points. From the predicted postoperative trunk shape in the first, second and third row of images, we can see that the models produce sharp, unrealistic edges or noisy protrusions where the underlying point cloud data is sparse or irregular. Smoothness loss helps to overcome such irregularities by promoting more coherent surface generation. We can also see a bump on the lower right surface of the predicted image in the first row that do not align with the ground truth postoperative trunk image.

Here, for the quantitative validation, the Chamfer distance of 0.3416 further quantifies the discrepancies between the predicted and ground truth postoperative shapes, emphasizing the need for smoothness loss to enhance the accuracy and realism of the predictions.

For Experiment 3 (without Density Loss):

Table 4.11 demonstrates the visualizations of the resulting trunk surface without density loss. We can observe some hollow areas or unnaturally thick regions on the surface of the trunk in the first, second and third row of postoperative predicted trunk images. Also, without the pressure to maintain density, the model does not totally preserve the fullness of regions such as the back, leading to a less realistic reconstruction. Additionally, from the three rows of images, it can be observed that around some areas such as the spinal column and the sides of the trunk that require a consistent density to capture detailed structures accurately in the predicted postop models, also lose definition and are not as distinguishable or anatomically correct.

The increased Chamfer distance of 0.3925 quantitatively displays the impact of excluding density loss from the loss function, indicating a greater deviation from the ground truth postoperative shape compared to experiments that include density loss.

For Experiment 4 (without Shape Loss):

The absence of shape loss depicted in the Table 4.12 of postop visualizations shows geometric distortions in the trunk's structure. Since shape loss guides the accuracy of the model's form, not including it results in incorrect curvatures and angles that do not correspond well with the actual

postoperative expectations. Without the constraints imposed by shape loss to maintain accurate proportions and positions, the trunk model might not accurately reflect the patient's true postoperative anatomy. The trunk model shows an inconsistency in maintaining the integrity of larger structural features. As we can see that the spinal column, the trunk edges and the overall anatomical trunk shape are not well-represented in the predicted postoperative trunk images without the shape loss.

The quantitative validation further supports this observation, with a higher Chamfer distance of 0.7873, indicating a substantial deviation from the ground truth postoperative shape. This highlights the importance of shape loss in achieving accurate and realistic reconstructions of postoperative trunk shapes.

Overall, the absence of each loss component individually highlights their respective contributions in the predictions of the postoperative trunk shapes. Smoothness loss ensures smooth transitions and coherence, density loss maintains uniform point distribution and preserves structural integrity, and shape loss contributes in the accuracy in the formation of the trunk shape.

In summary, we can infer that the inclusion of all the loss components is essential for achieving the most accurate and realistic reconstruction of the postoperative trunk shape. Shape loss has the most impact on the model's accuracy, followed by density loss and smoothness loss.

4.4 Extraction of Clinical Indices

The extraction of clinical indices such as Back Surface Rotation (BSR), Trunk Rotation (TR), Coronal Trunk Deviation (CTD), Sagittal Trunk Deviation (STD), and Depth Asymmetry (DA) is vital for evaluating the postoperative shape of the trunk in scoliosis patients. These indices provide quantitative measures of the spinal and trunk deformities, which are crucial for assessing the effectiveness of surgical interventions. BSR and TR give insights into the rotational correction, CTD and STD assess the alignment in the coronal and sagittal planes, and DA evaluates the symmetry of the trunk. By extracting these indices from the predicted postoperative shape, we can compare the predicted outcomes with the actual postoperative results, thus clinically validating the accuracy of the prediction model. We extract the max values for each of the clinical indices.

This post-processed predicted postoperative point cloud is given as input to the Torso3D application to measure these clinical indices. These measurements are applied on the predicted postop and the real postop trunk shape and these measurements are compared to evaluate the predicted postop trunk shape. The difference in the measurements conveys the effectiveness of the deep learning model in predicting postoperative trunk shapes. Smaller differences indicate a higher accuracy of the prediction.

Measurements of the trunk shape are plotted and their values are displayed in Figure 4.1. The graphical user interface (GUI) of Torso 3D was developed using MATLAB 7.12 which facilitates the visualization and analysis of 3D reconstructions of the trunk, its cross-sectional views, and four functional measurements [29].

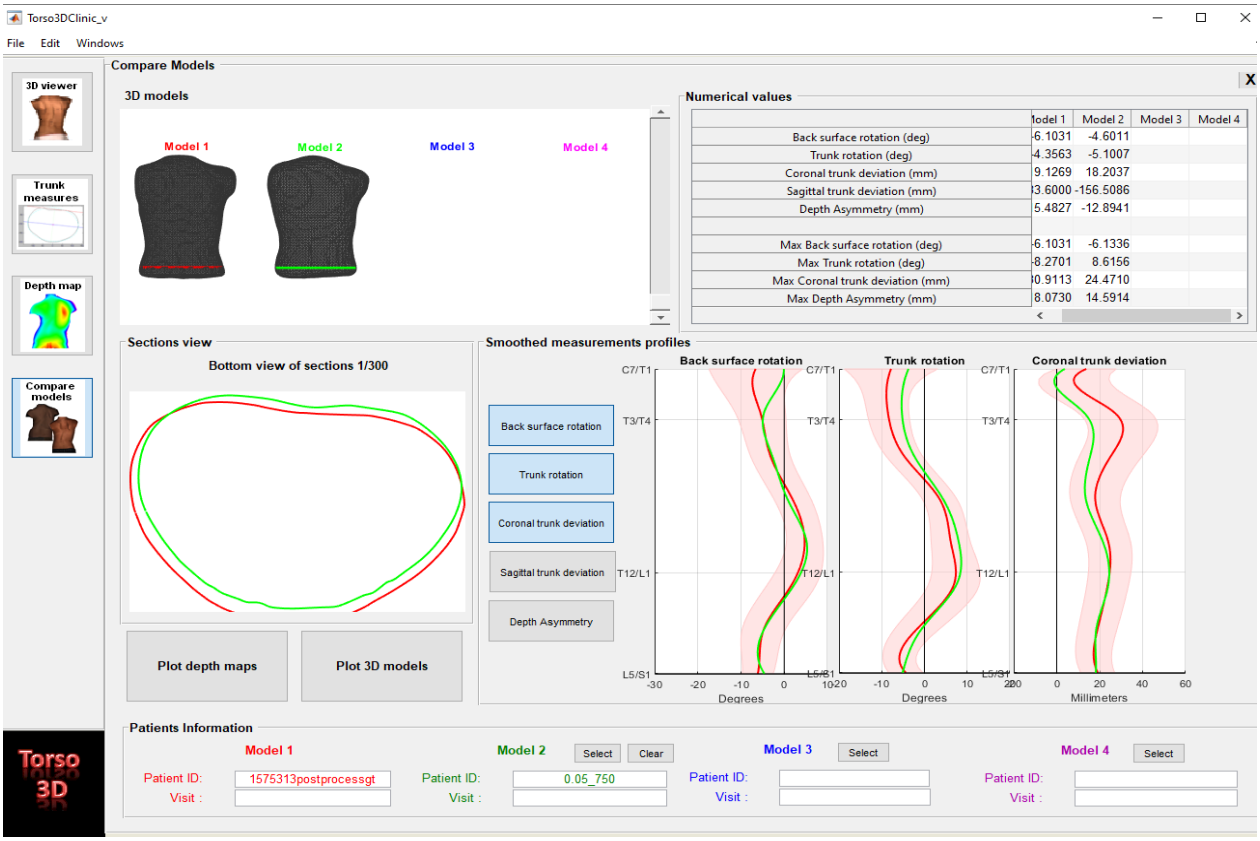

Figure 4.1 Torso 3D- Graphical User Interface to view measurements by using the slider (top left). Bottom left: sections of the trunk seen from below. Top right: Calculated Measurements of the trunk. Bottom Right: Curves representing measurements along the trunk for each acquisition. The two colors represent two different sources (Red: InSpeck, Green: Predicted postop trunk shape).

Hump Sum:

The Hump Sum is a measure used to quantify the asymmetry of the trunk. It is calculated by dividing the trunk into 100 sections along its length and measuring the depth asymmetry in each section. The depth asymmetry is a measure of the difference in depth between the two sides of the trunk at each section. The Hump Sum is the sum of these depth asymmetry measurements across all 100 sections [29]. The Hump Sum will be measured for the Best case and the Worst case scenario from the test cases in the following sections.

4.5 Clinical and Quantitative Validation

The value of each parameter in Table 4.13 is the absolute value of difference for each pair between the ground truth and the predicted trunk surfaces and the average of 32 cases from the test set. We considered two regions of the trunk i.e. the Thoracic region and the Lumbar region for analysing the values and obtained the Absolute difference of values for max values for each of the parameter.

Table 4.13 Absolute difference of values for all parameters

Parameters (Max Values)	Values
Back Surface Rotation (Thoracic) (deg)	2.56
Back Surface Rotation (Lumbar) (deg)	2.41
Trunk rotation (Thoracic) (deg)	2.29
Trunk rotation (Lumbar) (deg)	2.17
Coronal trunk Deviation (mm)	5.86
Sagittal Trunk Deviation (mm)	6.26
Depth Asymmetry (Thoracic) (mm)	3.91
Depth Asymmetry (Lumbar) (mm)	2.52

Table 4.14 Standard Deviation Value for each parameter

Parameters (Max Values)	Standard Deviation Values
Back Surface Rotation (Thoracic) (deg)	2.27
Back Surface Rotation (Lumbar) (deg)	1.74
Trunk rotation (Thoracic) (deg)	2.01
Trunk rotation (Lumbar) (deg)	1.69
Coronal trunk Deviation (mm)	4.15
Sagittal Trunk Deviation (mm)	5.89
Depth Asymmetry (Thoracic) (mm)	4.11
Depth Asymmetry (Lumbar) (mm)	2.34

4.5.1 Analysis for each parameter value

Back Surface Rotation (deg): The average absolute difference in the rotational angle of the back surface is 2.56° for the Thoracic region and 2.41° for the Lumbar region.

Trunk Rotation (deg): In this case, the rotational angle of the trunk is 2.29° for the Thoracic region and 2.17° for the Lumbar Region.

Coronal Trunk Deviation (mm): The average absolute difference in the lateral deviation of the trunk in the coronal plane is 5.86 mm.

Sagittal Trunk Deviation (mm): The average absolute difference in the deviation of the trunk in the sagittal plane is 6.26 mm. This is the largest deviation among the parameters, indicating that predicting the forward or backward bending of the trunk is more challenging.

Depth Asymmetry (mm): The average absolute difference in the depth asymmetry of the trunk is 3.91 mm for the Thoracic region and 2.52 mm for the Lumbar region. This parameter measures the asymmetry in the depth of the trunk, such as the prominence of the ribs or shoulder blade.

Standard Deviation Values for each parameter:

The standard deviation from Table 4.14 serves as a key metric to quantify the variability or spread of the absolute differences in prediction errors across the 32 cases for each parameter. A smaller standard deviation indicates that the prediction errors are more consistent across the cases, while a larger standard deviation suggests greater variability in the errors.

The analysis of standard deviations compared to average absolute differences across various parameters indicates low variability and consistent performance across the model's predictions. Most predictions show minimal deviation from the true values in a constrained manner. This consistency suggests that the error values are clustered around the mean, which points to a reliable and predictable model behavior.

4.5.2 Typical Error Measurement for the clinical indices

The typical error measurement reported in the paper [29] shows measurements between 1.20° and 2.05° for BSR and between 1.40° and 2.20° for TR. For coronal trunk deviation it is reported as between 2.9 mm to 6 mm and for sagittal trunk deviation it is shown between 2.5 mm to 5.5 mm.

Based on these typical error measurements, we can evaluate the absolute differences of the clinical parameters that we obtained as follows:

- For BSR, the model's average absolute difference value is 2.56° for Thoracic region and 2.41° for Lumbar region, which is slightly above the reported typical error range of 1.20° to 2.05°.
- For TR, the model's average absolute difference value for thoracic region is 2.29° and for the Lumbar region is 2.17°, which is slightly above the reported typical error range of 1.40° to 2.20° for Thoracic region and falls within this range for the Lumbar region.
- For CTD, the model's average absolute difference value is 5.86 mm, which is within the reported typical error range of 2.9 mm to 6 mm. This suggests that the model's predictions for CTD are within the acceptable range of typical error measurements.
- For STD, the model's average absolute difference value is 6.26 mm, which is slightly above the reported typical error range of 2.5 mm to 5.5 mm.

4.5.3 Quantitative Validation

We evaluate the performance of our PointNet++ model in predicting the postoperative trunk shape, using the Chamfer Distance (CD) as the primary quantitative metric. Since, the point coordinates are in the range of [0, 1], the Chamfer distance will be in the range of [0, 3] where, a Chamfer distance 0 indicates two point clouds are identical and a Chamfer distance of 3 indicates maximum distance apart and the point clouds are very different. Here, the Chamfer distance is obtained as 0.28 indicating that the predicted postoperative trunk shape is closer to the ground truth.

4.6 K-fold cross-validation Experiment

We also performed a K-fold cross-validation experiment using different subsets of the data as the validation set in each fold to get a more reliable estimate of the model's performance across various segments of the data.

A test set of 32 patients (20% of 158) is held out for final evaluation. In this approach, we consider $k = 5$. So, considering the other 126 patients dataset that we have, the dataset is divided into k folds, each fold takes turns being the validation set, while the remaining $k - 1$ folds serve as the training set. For each iteration (i.e., fold), one fold is designated as the validation set and the remaining four folds as the training set. The deep learning model is trained on the training set. This involves using the preoperative trunk shapes as inputs to predict the postoperative trunk shapes as in the case of earlier experiments. Then, the model is evaluated on the validation set by comparing the predicted postoperative trunk shapes with the ground truth where we use Chamfer distance metric to quantify the similarity between the predicted and actual point clouds.

Table 4.15 K-fold cross-validation experiment results

Preoperative	Predicted Postoperative	Ground Truth
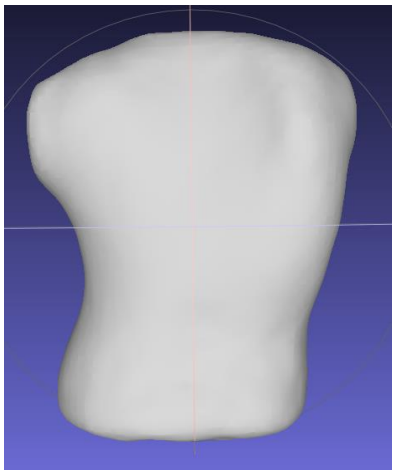	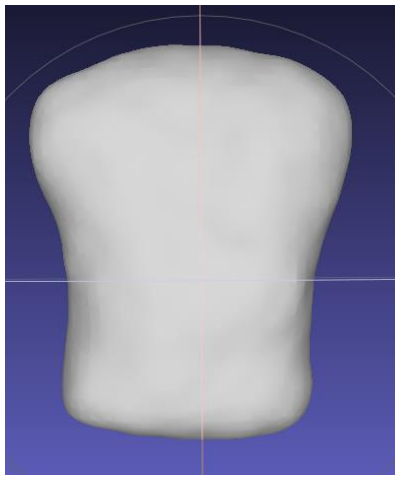	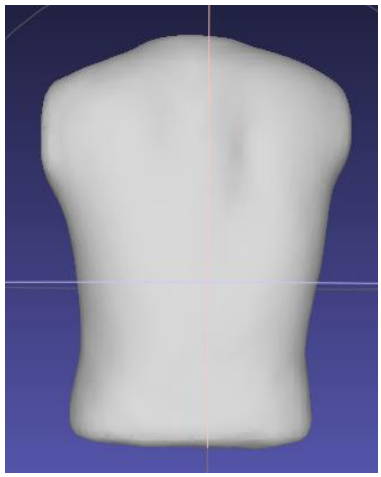
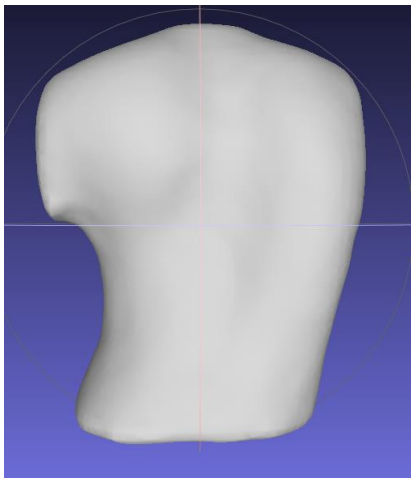	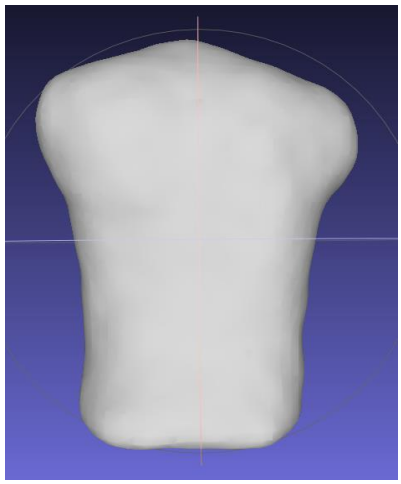	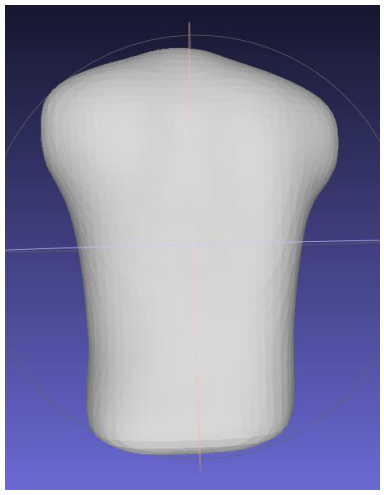
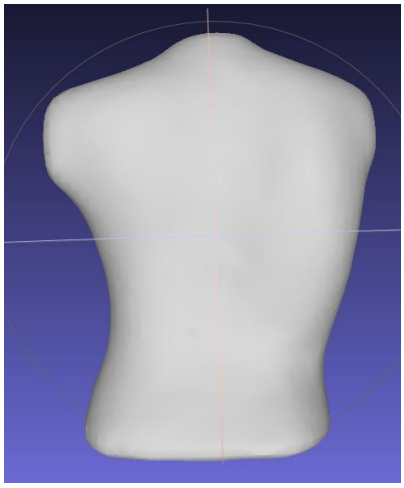	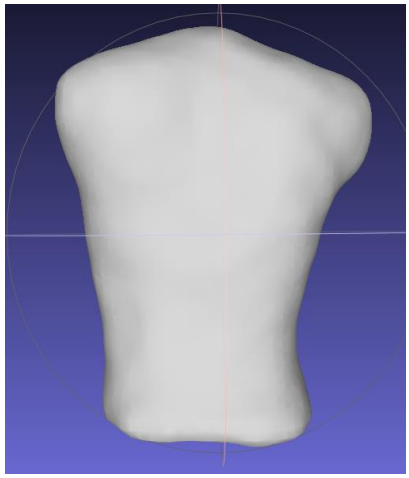	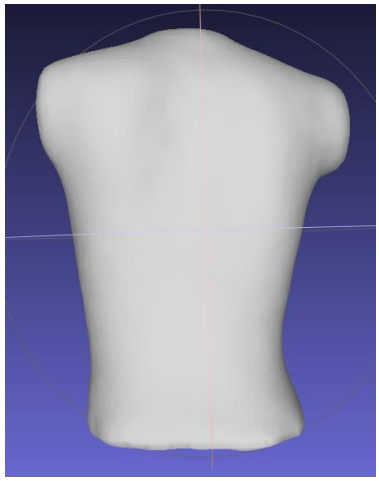

Table 4.16 Absolute difference of values for all parameters for K-fold experiment

Parameters (Max Values)	**Values**
Back Surface Rotation (Thoracic) (deg)	2.48
Back Surface Rotation (Lumbar) (deg)	2.37
Trunk rotation (Thoracic) (deg)	2.25
Trunk rotation (Lumbar) (deg)	2.14
Coronal trunk Deviation (mm)	5.83
Sagittal Trunk Deviation (mm)	6.22
Depth Asymmetry (Thoracic) (mm)	3.86
Depth Asymmetry (Lumbar) (mm)	2.45

Table 4.17 Standard Deviation Value for each parameter

Parameters (Max Values)	**Standard Deviation Values**
Back Surface Rotation (Thoracic) (deg)	2.24
Back Surface Rotation (Lumbar) (deg)	1.73
Trunk rotation (Thoracic) (deg)	1.97
Trunk rotation (Lumbar) (deg)	1.68
Coronal trunk Deviation (mm)	4.09
Sagittal Trunk Deviation (mm)	5.83
Depth Asymmetry (Thoracic) (mm)	4.07
Depth Asymmetry (Lumbar) (mm)	2.32

The Chamfer distance for this k-fold cross-validation experiment is found to be slightly improved over the train-test-validation experiment in section 4.2. By averaging the Chamfer distance metric

over five folds, k-fold cross-validation reduces the bias that could be present in a single train-test split and the value is 0.26 as compared to the value in the aforementioned experiment as 0.28.

Also, from the visualization results in Table 4.15 and the parameter values of the clinical indices in Table 4.14, we can see some slight improvements across the absolute values for all the parameters. Since k-fold cross-validation involves using every part of the dataset for both training and validation, the model is thoroughly tested on all available data. This comprehensive validation process leads to a slightly more accurate assessment of the model's performance and better optimization of clinical indices like BSR, TR, CTD, STD, and DA.

From the values in Table 4.17, we can see that the standard deviation values for most parameters have slightly decreased after performing the k-fold cross-validation experiment. This suggests that the model's predictions have become more consistent across the test cases.

4.7 Comparison of our experiment with previous work

A simulation approach for predicting the trunk's external appearance after the surgery was presented in [33]. Our proposed work shows the deep learning approach for predicting the postoperative shape of the trunk.

We consider the same patients as in [33] as a test set consisting of 7 patients, the model is trained on the remaining 151 data and evaluated with the measurement of the back surface rotation (BSR) as indicated in the work.

The mean absolute error of the BSR index measured on the simulated trunks ranges from 1.20° (±0.73°) to 3.2° (±0.83°) in the thoracic region.

For the Lumbar region, the mean absolute error ranges from 2.32° (±2.26°) to 7.45° (±3.10°) for the simulated results [33].

Our results obtained from the deep learning model:

For the Thoracic region, the mean absolute error obtained for BSR is: 3.11° (± 1.23)

For the Lumbar region, the mean absolute error obtained for BSR is: 4.04° (± 1.19)

We can see that the deep learning model's mean absolute error for the Thoracic region as well as the Lumbar region falls within the given range and is comparable to the simulated results.

This suggests that the model results are comparable as that of the of traditional simulations.

4.8 Best case and Worst case

The best case and the worst case of the predicted postop shape of the trunk among the 32 test cases is illustrated in Figure 4.2 and Figure 4.4 in Torso 3D. The procedure of calculation is as follows:

- Compute Absolute Differences: For each test case, the absolute difference between the predicted and ground truth values for each parameter (BSR, TR, CTD, STD, and DA) is calculated. This gives the absolute difference for each parameter in each test case.
- Calculate Relative Error Percentage: For each parameter in each test case, calculate the relative error percentage by dividing the absolute error by the ground truth value and then multiplying by 100 to get the percentage.
- Sum Relative Errors: For each test case, sum up the relative error percentages of all parameters to get the total relative error percentage for that test case.
- Best and Worst Case Selection:
    - The best case of the model is the one with the lowest total relative error percentage (see Figure 4.2).
    - The worst case of the model is the one with the highest total relative error percentage (see Figure 4.4).

4.8.1 Best Case

Also, in Figure 4.2 we can see that visually the curves representing the actual and predicted values for each clinical index are closely aligned. This means that for each patient or case, the predicted value of a particular index is very close to the actual value. This close alignment is observed consistently across all the clinical indices being considered.

From Figure 4.3 indicating the comparison between the ground truth postop (Model 1) and predicted postop (Model 2) of Hump sum in the best case scenario, we can see that there is a

deviation of 55 mm between the ground truth and the predicted Hump Sum. This indicates that the predicted postoperative shape of the trunk is less asymmetrical than the actual postoperative shape.

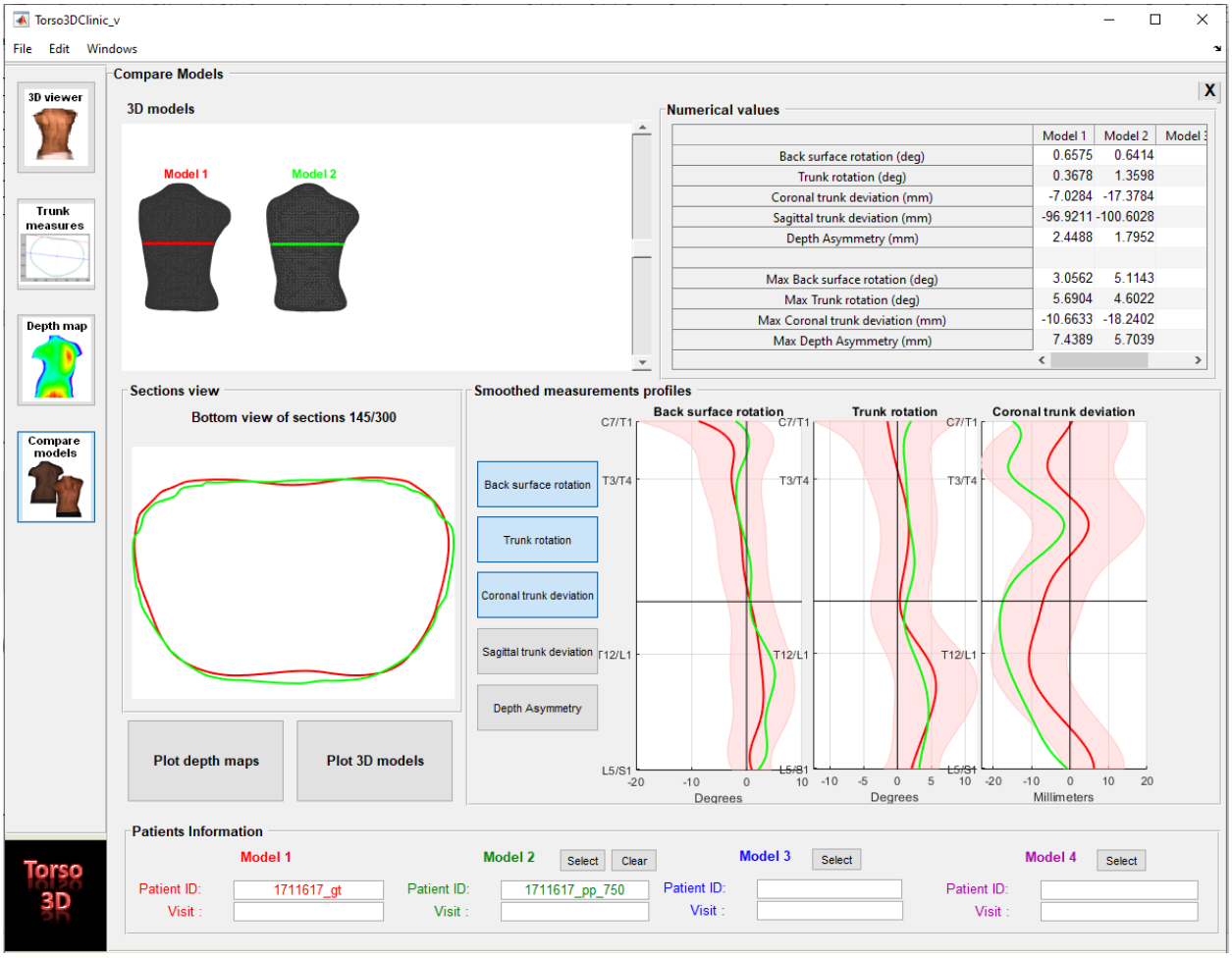

Figure 4.2 Best case postop prediction

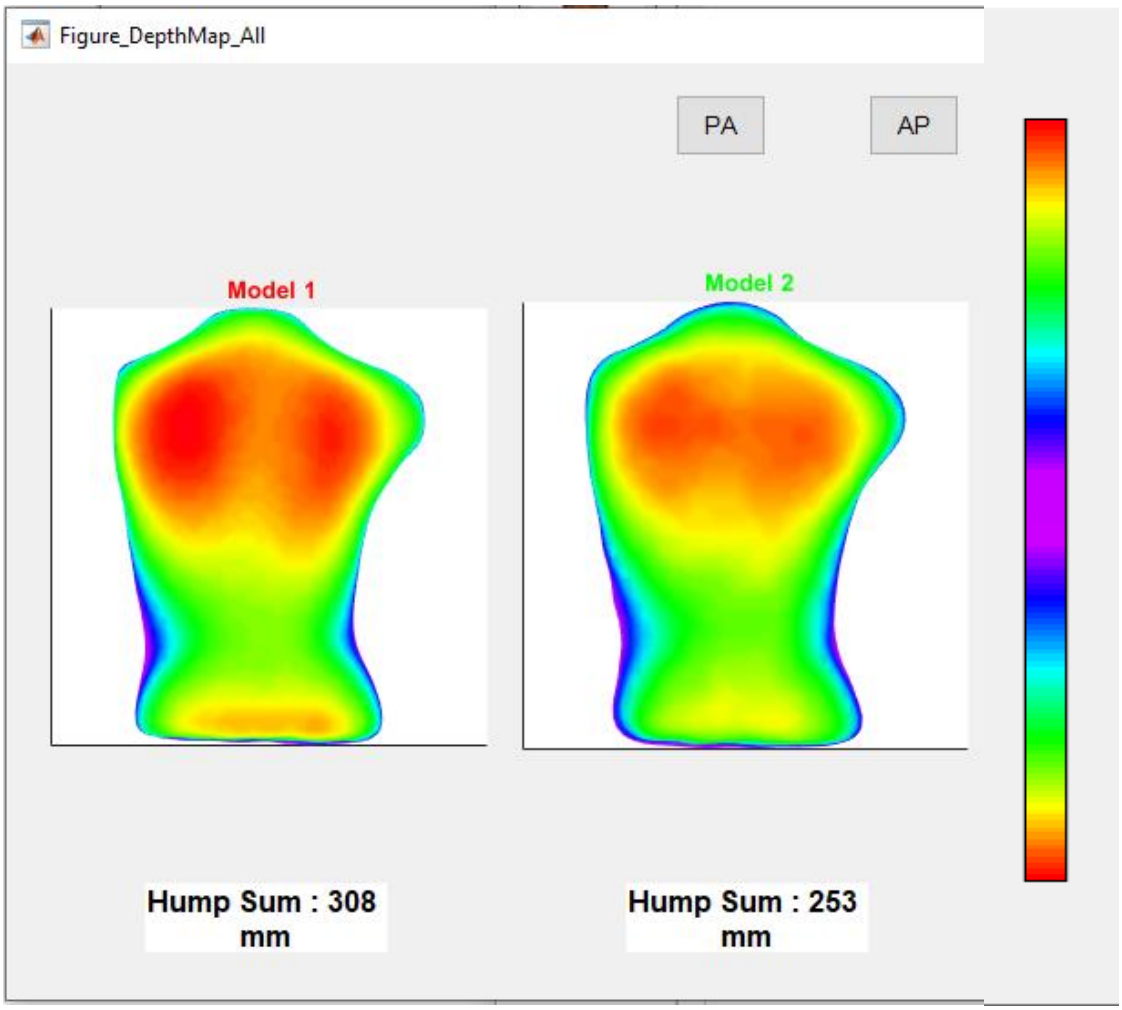

Figure 4.3 Depth Map for Best case

4.8.2 Worst Case

From Figure 4.4, we can observe that the curves representing the actual and predicted values for each clinical index show noticeable differences. This represents that for each patient or case, the predicted value of a particular index does not closely match the actual value. The differences between the actual and predicted values are evident from a visual inspection of the curves.

Figure 4.5 shows the Hump sum in the worst case scenario where the discrepancy of 534 mm indicates a high divergence between the predicted and actual outcomes.

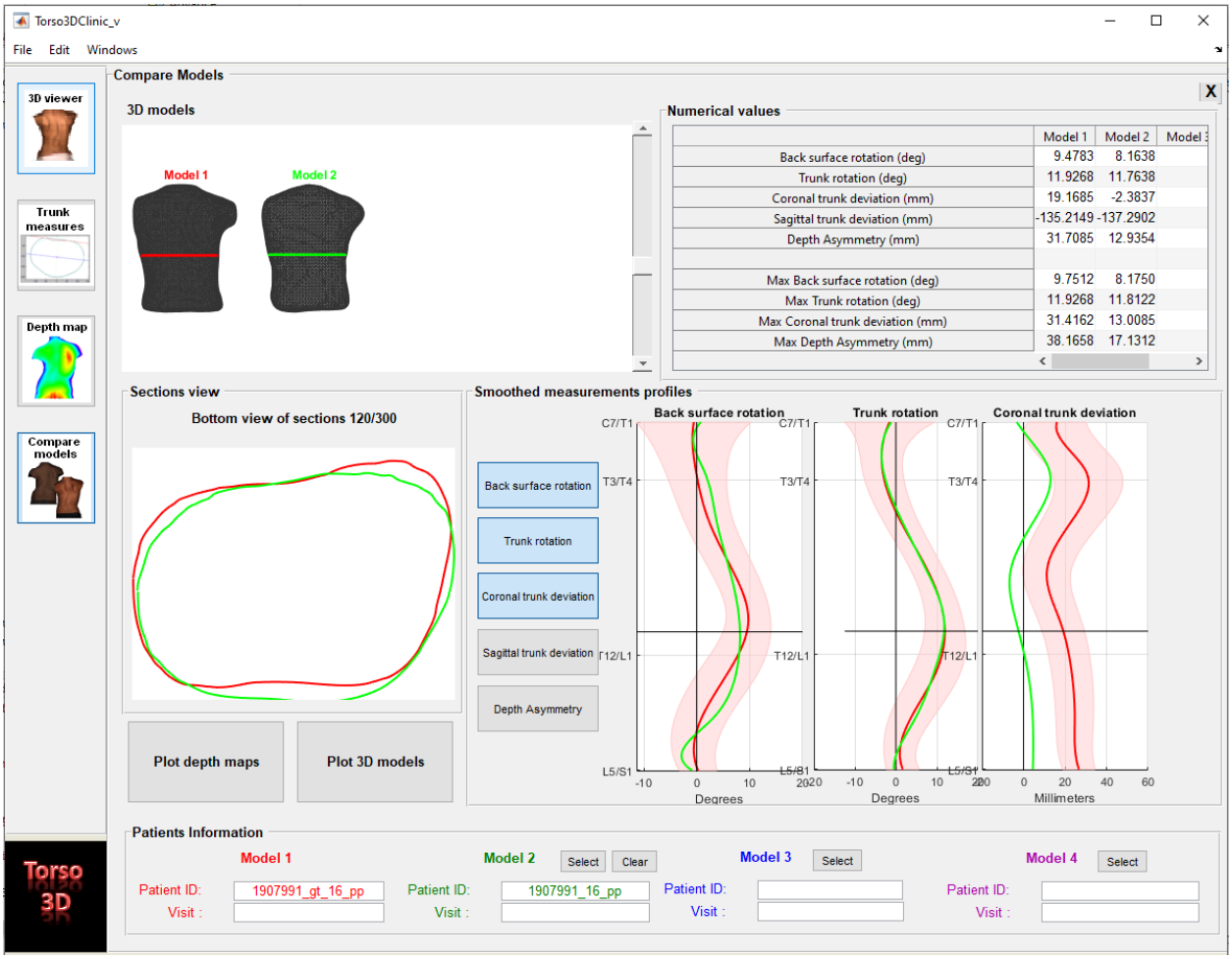

Figure 4.4 Worst case postop prediction

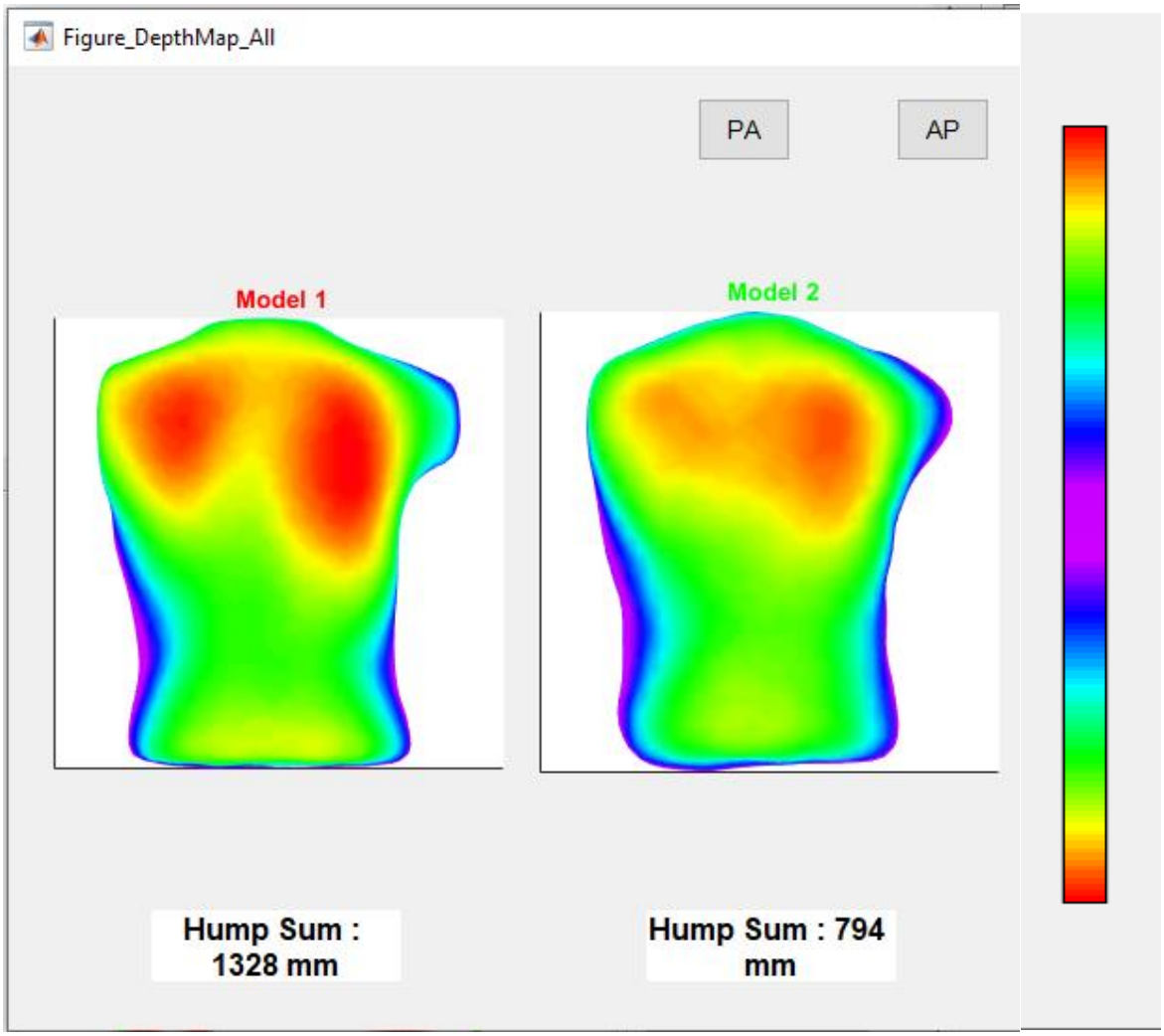

Figure 4.5 Depth map for Worst case

4.9 General Discussion

The results of this study demonstrate the potential of a deep learning approach, specifically using an architecture considering PointNet++ network as its backbone, for predicting the postoperative shape of the trunk in patients with Adolescent Idiopathic Scoliosis (AIS). The postprocessing step involving MeshLab's Poisson surface reconstruction is crucial for transforming the raw point cloud output into a continuous trunk surface, providing a more accurate and visually comprehensible representation of the trunk shape.

A finer parameter tuning both for the weights of the loss and the post-processing is necessary and could improve on the results. The weights of the loss function components (shape, density, and smoothness loss) is critical in guiding the learning process.

Computing normals for a set of points is a critical step in reconstructing a surface from point cloud data, in the context of Poisson Surface Reconstruction. The 'Number of Neighbors' parameter is integral to the process of normal computation. If too few neighbors are used, the normal estimation can be noisy, especially if the point cloud is not dense. If too many neighbors are used, the estimated normals might be too smoothed out, potentially blurring out fine details in the reconstructed surface. Hence, considering suitable parameter for the number of neighbors is an important aspect and needs to be carefully considered.

The ablation study highlights the importance of different components of the loss function. It shows that incorporating all loss components, including shape loss, density loss, and smoothness loss, is essential for achieving the most accurate and realistic reconstruction of the postoperative trunk shape. The exclusion of any of these components leads to noticeable deficiencies in the predicted shape, such as rough surfaces, irregular surface distributions, or geometric distortions.

Extraction of clinical indices like Back Surface Rotation, Trunk Rotation, Coronal Trunk Deviation, Sagittal Trunk Deviation, and Depth Asymmetry is vital for evaluating the model's predictions against clinical standards. The relatively small differences between the predicted and actual values of these indices suggest that the deep learning model is effective in capturing the key aspects of postoperative trunk shape.

We also compared the average absolute differences obtained from our model with typical error measurements reported in the literature. Our model's average absolute differences for Back Surface Rotation (BSR), Trunk Rotation for Thoracic region and Sagittal Trunk Deviation (STD) were slightly above the typical ranges, indicating a room for improvement. However, for Trunk Rotation (TR) in the Lumbar region and Coronal Trunk Deviation (CTD), our model's performance fell within the expected error ranges.

The k-fold cross-validation experiment further supports the reliability of the model across different data segments. The slight improvement in Chamfer distance and clinical indices in this experiment indicates better performance of the model.

With respect to our deep learning model’s comparison with [33], the model’s performance in the Thoracic region and Lumbar region, where it shows a mean error well within the expected range, indicates its potential reliability for clinical use. Since that the model's errors fall within typical simulation ranges, it could be considered for clinical applications, particularly in preoperative planning where understanding potential postoperative outcomes is crucial.

The identification of the best and worst cases based on the sum of relative error percentage across all parameters provides insight into the model's performance range. The close alignment of curves in the best case scenario indicates a high level of accuracy in the predictions, while the noticeable differences in the worst case scenario highlight areas for improvement.

While the model's predictions were quantitatively validated against clinical indices, there is a need for a more in-depth analysis of the results. Understanding how the predictions vary with patient demographics, curve types, or specific surgical procedures could reveal underlying patterns that the model is capturing or missing. This kind of analysis might uncover biases or areas where the model particularly excels or struggles.

In summary, the findings of this study emphasize the potential of deep learning models in aiding preoperative planning and outcome prediction for scoliosis surgery.

CHAPTER 5 CONCLUSION

In conclusion, we successfully proposed a deep learning architecture model, utilizing the PointNet++ network, to predict the postoperative shape of the trunk in patients with scoliosis. The methodology encompassed several steps, starting with using the Full Body Surface Topography (FBST) data, followed by preprocessing steps including downsampling and normalization to prepare the data for the deep learning model. The architecture of the proposed model was chosen to effectively handle point cloud data and capture both local and global features of the trunk's shape, which is essential for accurate shape prediction.

We also did the ablation study as part of this research which provided valuable insights into the performance of the learning model, highlighting the importance of each component in the loss function, which included shape loss, point-density loss, and smoothness loss. These components collectively guided the model's training process to ensure the transformation of the preoperative trunk shape to the postoperative shape.

Furthermore, we also performed a k-fold cross-validation experiment for the purpose of model evaluation, which shows reliability and generalizability across different subsets of the dataset.

The extraction of clinical indices from the predicted postoperative shape provided a quantifiable measure of the trunk's shape, which is crucial for evaluating the surgical outcome and planning further treatment.

Finally, the quantitative validation using Chamfer distance and clinical indices ensures the accuracy and reliability of the predicted postoperative trunk shape. This validation is essential which makes it a promising tool for enhancing surgical planning and patient care in the context of scoliosis treatment.

The deep learning model demonstrates promising accuracy levels that are consistent with those obtained from traditional simulation methods. This highlights the potential of deep learning techniques in enhancing predictive analytics in surgical planning. Further validation and refinement could make this model a valuable tool in clinical settings, particularly for surgeries involving the spine where precise outcome predictions are essential.

While the methodology and results of this study are promising, there exists certain limitations.

As the human trunk's shape is complex and varies significantly between individuals, capturing all the nuances of this shape, especially the subtle changes post-surgery, can be challenging for any model, including PointNet++.

From the experiments, we can also notice the challenge in accurately predicting forward or backward bending of the trunk (as indicated by the larger deviation in Sagittal Trunk Deviation), suggesting a limitation in the model's ability to preserve or predict finer anatomical details. This could arise from the inherent complexity of capturing such fine details solely from point cloud data or maybe the limitations in the current architecture's capacity to learn these features effectively.

The future work of this project could include incorporating the spine in the input to assess possible improvement in the results. It could potentially provide more anatomical context and improve the accuracy of the postoperative trunk shape predictions. This could lead to a more comprehensive understanding of the surgical outcomes and enhance the ability for surgical plans to individual patients' needs. Additionally, the inclusion of additional data, such as patient demographic details or more specific information about the surgical procedure, could improve the model's predictive power.

REFERENCES

[1] S. Parent, P. O. Newton, and D. R. Wenger, “Adolescent idiopathic scoliosis: etiology, anatomy, natural history, and bracing,” *Instr. Course Lect.*, vol. 54, pp. 529–536, 2005.

[2] G. S. Motyer, P. J. Kiely, and A. Fitzgerald, “Adolescents’ Experiences of Idiopathic Scoliosis in the Presurgical Period: A Qualitative Study,” *J. Pediatr. Psychol.*, vol. 47, no. 2, pp. 225–235, Sep. 2021, doi: 10.1093/jpepsy/jsab095.

[3] C. E. Aubin, H. Labelle, C. Chevrefils, G. Desroches, J. Clin, and A. B. M. Eng, “Preoperative Planning Simulator for Spinal Deformity Surgeries,” *Spine*, vol. 33, no. 20, p. 2143, Sep. 2008, doi: 10.1097/BRS.0b013e31817bd89f.

[4] M. Asher, S. Min Lai, D. Burton, and B. Manna, “The reliability and concurrent validity of the scoliosis research society-22 patient questionnaire for idiopathic scoliosis,” *Spine*, vol. 28, no. 1, pp. 63–69, Jan. 2003, doi: 10.1097/00007632-200301010-00015.

[5] L. Y. Carreon, J. O. Sanders, M. Diab, P. F. Sturm, D. J. Sucato, and the S. D. S. Group, “Patient Satisfaction After Surgical Correction of Adolescent Idiopathic Scoliosis,” *Spine*, vol. 36, no. 12, p. 965, May 2011, doi: 10.1097/BRS.0b013e3181e92b1d.

[6] O. Dionne, K. C. Assi, S. Grenier, H. Labelle, F. Guibault, and F. Cheriet, “Simulation of the postoperative trunk appearance in scoliosis surgery,” in *2012 9th IEEE International Symposium on Biomedical Imaging (ISBI)*, Barcelona, Spain: IEEE, May 2012, pp. 1208–1211. doi: 10.1109/ISBI.2012.6235778.

[7] R. K. Pratt, J. K. Webb, R. G. Burwell, and A. A. Cole, “Changes in Surface and Radiographic Deformity After Universal Spine System for Right Thoracic Adolescent Idiopathic Scoliosis: Is Rib-Hump Reassertion a Mechanical Problem of the Thoracic Cage Rather Than an Effect of Relative Anterior Spinal Overgrowth?,” *Spine*, vol. 26, no. 16, p. 1778, Aug. 2001.

[8] L. Seoud, F. Cheriet, H. Labelle, and S. Parent, “Changes in Trunk Appearance After Scoliosis Spinal Surgery and Their Relation to Changes in Spinal Measurements,” *Spine Deform.*, vol. 3, no. 6, pp. 595–603, Nov. 2015, doi: 10.1016/j.jspd.2015.05.001.

[9] L. Seoud, “Analyse de la relation entre les déformations scoliotiques deu tronc et celles des structures osseuses sous-jacente,” Thèse de doctorat, Institut de génie biomédicale, École Polytechnique de Montréal, Montreal, QC, 2012.

[10] P. Trobisch, O. Suess, and F. Schwab, “Idiopathic scoliosis,” *Dtsch. Arzteblatt Int.*, vol. 107, no. 49, pp. 875–883; quiz 884, Dec. 2010, doi: 10.3238/arztebl.2010.0875.

[11] W. K. Payne, J. W. Ogilvie, M. D. Resnick, R. L. Kane, E. E. Transfeldt, and R. W. Blum, “Does scoliosis have a psychological impact and does gender make a difference?,” *Spine*, vol. 22, no. 12, pp. 1380–1384, Jun. 1997, doi: 10.1097/00007632-199706150-00017.

[12] D. Youstina, “Évaluation de la précision de systèmes d’acquisition de la géométrie 3D du tronc pour la conception de corsets personnalisés,” Mémoire de Maîtrise, Institut de génie biomédicale, École Polytechnique de Montréal, Montreal, QC, 2020.

[13] “An objective criterion for scoliosis screening. : JBJS.” Accessed: Mar. 21, 2024. [Online]. Available: https://journals.lww.com/jbjsjournal/Abstract/1984/66090/An_objective_criterion_for_scoliosis_screening_.10.aspx

[14] “Braces Optimized With Computer-Assisted Design and Simulations Are Lighter, More Comfortable, and More Efficient Than Plaster-Cast Braces for the Treatment of Adolescent Idiopathic Scoliosis - ScienceDirect.” Accessed: Mar. 22, 2024. [Online]. Available: https://www.sciencedirect.com/science/article/abs/pii/S2212134X14000343?via%3Dihub

[15] J. E. Lonstein, “Adolescent idiopathic scoliosis,” *Lancet Lond. Engl.*, vol. 344, no. 8934, pp. 1407–1412, Nov. 1994, doi: 10.1016/s0140-6736(94)90572-x.

[16] S. L. Weinstein, L. A. Dolan, J. C. Cheng, A. Danielsson, and J. A. Morcuende, “Adolescent idiopathic scoliosis,” *The Lancet*, vol. 371, no. 9623, pp. 1527–1537, May 2008, doi: 10.1016/S0140-6736(08)60658-3.

[17] “Effects of Bracing in Adolescents with Idiopathic Scoliosis | NEJM.” Accessed: Mar. 22, 2024. [Online]. Available: https://www.nejm.org/doi/full/10.1056/NEJMoa1307337

[18] D. Fortin, F. Cheriet, M. Beauséjour, P. Debanné, J. Joncas, and H. Labelle, “A 3D visualization tool for the design and customization of spinal braces,” *Comput. Med. Imaging Graph. Off. J. Comput. Med. Imaging Soc.*, vol. 31, no. 8, pp. 614–624, Dec. 2007, doi: 10.1016/j.compmedimag.2007.07.006.

[19] H. Labelle, C. Bellefleur, J. Joncas, C.-É. Aubin, and F. Cheriet, “Preliminary Evaluation of a Computer-Assisted Tool for the Design and Adjustment of Braces in Idiopathic Scoliosis: A Prospective and Randomized Study,” *Spine*, vol. 32, no. 8, p. 835, Apr. 2007, doi: 10.1097/01.brs.0000259811.58372.87.

[20] “TOWARDS THE SELF-CALIBRATION OF A MULTIVIEW RADIOGRAPHIC IMAGING SYSTEM FOR THE 3D RECONSTRUCTION OF THE HUMAN SPINE AND RIB CAGE | International Journal of Pattern Recognition and Artificial Intelligence.” Accessed: Mar. 22, 2024. [Online]. Available: https://www.worldscientific.com/doi/abs/10.1142/S0218001499000434

[21] K. H. Bridwell, “Surgical Treatment of Idiopathic Adolescent Scoliosis,” *Spine*, vol. 24, no. 24, p. 2607, Dec. 1999.

[22] C. Bellefleur, J. Dansereau, A. Koller, and H. Labelle, “Evaluation of the efficiency of patient stabilization devices for 3D X-ray reconstruction of the spine and rib cage,” *Stud. Health Technol. Inform.*, vol. 88, pp. 127–131, 2002.

[23] F. Cheriet, C. Laporte, S. Kadoury, H. Labelle, and J. Dansereau, “A novel system for thE 3-D reconstruction of the human spine and rib cage from biplanar X-ray images,” *IEEE Trans. Biomed. Eng.*, vol. 54, no. 7, pp. 1356–1358, Jul. 2007, doi: 10.1109/TBME.2006.889205.

[24] S. Kadoury, F. Cheriet, C. Laporte, and H. Labelle, “A versatile 3D reconstruction system of the spine and pelvis for clinical assessment of spinal deformities,” *Med. Biol. Eng. Comput.*, vol. 45, no. 6, pp. 591–602, Jun. 2007, doi: 10.1007/s11517-007-0182-1.

[25] “Assessment of the 3-D reconstruction and high-resolution geometrical modeling of the human skeletal trunk from 2-D radiographic images | IEEE Journals & Magazine | IEEE Xplore.” Accessed: Mar. 22, 2024. [Online]. Available: https://ieeexplore.ieee.org/document/1213851

[26] V. Pazos, F. Cheriet, L. Song, H. Labelle, and J. Dansereau, “Accuracy assessment of human trunk surface 3D reconstructions from an optical digitising system,” *Med. Biol. Eng. Comput.*, vol. 43, no. 1, pp. 11–15, Feb. 2005, doi: 10.1007/BF02345117.

[27] K. C. Assi, H. Labelle, and F. Cheriet, “Statistical model based 3D shape prediction of postoperative trunks for non-invasive scoliosis surgery planning,” *Comput. Biol. Med.*, vol. 48, pp. 85–93, May 2014, doi: 10.1016/j.compbiomed.2014.02.015.

[28] V. Pazos, F. Cheriet, J. Danserau, J. Ronsky, R. F. Zernicke, and H. Labelle, “Reliability of trunk shape measurements based on 3-D surface reconstructions,” *Eur. Spine J.*, vol. 16, no. 11, pp. 1882–1891, Nov. 2007, doi: 10.1007/s00586-007-0457-0.

[29] L. Seoud, J. Dansereau, H. Labelle, and F. Cheriet, “Multilevel Analysis of Trunk Surface Measurements for Noninvasive Assessment of Scoliosis Deformities,” *Spine*, vol. 37, no. 17, p. E1045, Aug. 2012, doi: 10.1097/BRS.0b013e3182575938.

[30] L. Seoud, F. Cheriet, H. Labelle, and S. Parent, “Non-invasive quantitative assessment of scoliosis spinal surgery outcome,” presented at the Progress in Biomedical Optics and Imaging - Proceedings of SPIE, Mar. 2013, p. 86721N. doi: 10.1117/12.2007515.

[31] C.-É. Aubin, J. Dansereau, F. Parent, H. Labelle, and J. A. de Guise, “Morphometric evaluations of personalised 3D reconstructions and geometric models of the human spine,” *Med. Biol. Eng. Comput.*, vol. 35, no. 6, pp. 611–618, Nov. 1997, doi: 10.1007/BF02510968.

[32] M. Robitaille, C.-É. Aubin, and H. Labelle, “Effects of alternative instrumentation strategies in adolescent idiopathic scoliosis: A biomechanical analysis,” *J. Orthop. Res.*, vol. 27, no. 1, pp. 104–113, 2009, doi: 10.1002/jor.20654.

[33] K. C. Assi, S. Grenier, S. Parent, H. Labelle, and F. Cheriet, “A physically based trunk soft tissue modeling for scoliosis surgery planning systems,” *Comput. Med. Imaging Graph.*, vol. 40, pp. 217–228, Mar. 2015, doi: 10.1016/j.compmedimag.2014.11.002.

[34] Y. Majdouline, C.-E. Aubin, A. Sangole, and H. Labelle, “Computer simulation for the optimization of instrumentation strategies in adolescent idiopathic scoliosis,” *Med. Biol. Eng. Comput.*, vol. 47, no. 11, pp. 1143–1154, Nov. 2009, doi: 10.1007/s11517-009-0509-1.

[35] D. Périé, C. E. Aubin, M. Lacroix, Y. Lafon, and H. Labelle, “Biomechanical modelling of orthotic treatment of the scoliotic spine including a detailed representation of the brace-torso interface,” *Med. Biol. Eng. Comput.*, vol. 42, no. 3, pp. 339–344, May 2004, doi: 10.1007/BF02344709.

[36] J. Carrier, C. E. Aubin, I. Villemure, and H. Labelle, “Biomechanical modelling of growth modulation following rib shortening or lengthening in adolescent idiopathic scoliosis,” *Med. Biol. Eng. Comput.*, vol. 42, no. 4, pp. 541–548, Jul. 2004, doi: 10.1007/BF02350997.

[37] J. Clin, C.-E. Aubin, S. Parent, J. Ronsky, and H. Labelle, “Biomechanical modeling of brace design,” *Stud. Health Technol. Inform.*, vol. 123, pp. 255–260, 2006.

[38] J. Clin, C.-É. Aubin, and H. Labelle, “Virtual prototyping of a brace design for the correction of scoliotic deformities,” *Med. Biol. Eng. Comput.*, vol. 45, no. 5, pp. 467–473, May 2007, doi: 10.1007/s11517-007-0171-4.

[39] J. Clin, C.-E. Aubin, S. Parent, A. Sangole, and H. Labelle, “Comparison of the biomechanical 3D efficiency of different brace designs for the treatment of scoliosis using a finite element model,” *Eur. Spine J. Off. Publ. Eur. Spine Soc. Eur. Spinal Deform. Soc. Eur. Sect. Cerv. Spine Res. Soc.*, vol. 19, no. 7, pp. 1169–1178, Jul. 2010, doi: 10.1007/s00586-009-1268-2.

[40] J. Clin, C.-E. Aubin, S. Parent, and H. Labelle, “A biomechanical study of the Charleston brace for the treatment of scoliosis,” *Spine*, vol. 35, no. 19, pp. E940-947, Sep. 2010, doi: 10.1097/BRS.0b013e3181c5b5fa.

[41] J. Clin, C.-E. Aubin, H. Labelle, and S. Parent, “Immediate correction required to expect a long-term effectiveness of a brace treatment: a biomechanical insight,” *Scoliosis*, vol. 5, no. 1, p. O63, Sep. 2010, doi: 10.1186/1748-7161-5-S1-O63.

[42] M. Beauséjour, C. E. Aubin, A. G. Feldman, and H. Labelle, “[Simulation of lateral bending tests using a musculoskeletal model of the trunk],” *Ann. Chir.*, vol. 53, no. 8, pp. 742–750, 1999.

[43] N. Lampen *et al.*, “Deep learning for biomechanical modeling of facial tissue deformation in orthognathic surgical planning,” *Int. J. Comput. Assist. Radiol. Surg.*, vol. 17, no. 5, pp. 945–952, May 2022, doi: 10.1007/s11548-022-02596-1.

[44] A. Odot, R. Haferssas, and S. Cotin, “DeepPhysics: a physics aware deep learning framework for real-time simulation.” arXiv, Sep. 17, 2021. doi: 10.48550/arXiv.2109.09491.

[45] S. U. Saeed, Z. A. Taylor, M. A. Pinnock, M. Emberton, D. C. Barratt, and Y. Hu, “Prostate motion modelling using biomechanically-trained deep neural networks on unstructured nodes.” arXiv, Jul. 09, 2020. doi: 10.48550/arXiv.2007.04972.

[46] M. Khani, P. Debanné, H. Labelle, S. Parent, and F. Cheriet, “Prediction of postoperative 3D spine shape using Controlled Point Deformation Network (CPDNet),” in *Medical Imaging 2023: Image Processing*, SPIE, Apr. 2023, pp. 668–674. doi: 10.1117/12.2654224.

[47] A. Mendizabal, E. Tagliabue, J.-N. Brunet, D. Dall’Alba, P. Fiorini, and S. Cotin, “Physics-Based Deep Neural Network for Real-Time Lesion Tracking in Ultrasound-Guided Breast Biopsy,” in *Computational Biomechanics for Medicine*, K. Miller, A. Wittek, G. Joldes, M. P. Nash, and P. M. F. Nielsen, Eds., Cham: Springer International Publishing, 2020, pp. 33–45. doi: 10.1007/978-3-030-42428-2_4.

[48] J.-N. Brunet, A. Mendizabal, A. Petit, N. Golse, E. Vibert, and S. Cotin, “Physics-based Deep Neural Network for Augmented Reality during Liver Surgery,” presented at the MICCAI 2019 - 22nd International Conference on Medical Image Computing and Computer Assisted Intervention, Springer, Oct. 2019, p. 8. doi: 10.1007/978-3-030-32254-0_16.

[49] A. Sanchez-Gonzalez, J. Godwin, T. Pfaff, R. Ying, J. Leskovec, and P. W. Battaglia, “Learning to Simulate Complex Physics with Graph Networks.” arXiv, Sep. 14, 2020. doi: 10.48550/arXiv.2002.09405.

[50] B. Yaman, S. A. H. Hosseini, S. Moeller, J. Ellermann, K. Uğurbil, and M. Akçakaya, “Self-Supervised Physics-Based Deep Learning MRI Reconstruction Without Fully-Sampled Data,” in *2020 IEEE 17th International Symposium on Biomedical Imaging (ISBI)*, Apr. 2020, pp. 921–925. doi: 10.1109/ISBI45749.2020.9098514.

[51] A. Balu, S. Nallagonda, F. Xu, A. Krishnamurthy, M.-C. Hsu, and S. Sarkar, “A Deep Learning Framework for Design and Analysis of Surgical Bioprosthetic Heart Valves,” *Sci. Rep.*, vol. 9, no. 1, Art. no. 1, Dec. 2019, doi: 10.1038/s41598-019-54707-9.

[52] R. Q. Charles, H. Su, M. Kaichun, and L. J. Guibas, “PointNet: Deep Learning on Point Sets for 3D Classification and Segmentation,” in *2017 IEEE Conference on Computer Vision and Pattern Recognition (CVPR)*, Honolulu, HI: IEEE, Jul. 2017, pp. 77–85. doi: 10.1109/CVPR.2017.16.

[53] C. R. Qi, L. Yi, H. Su, and L. J. Guibas, “PointNet++: Deep Hierarchical Feature Learning on Point Sets in a Metric Space.” arXiv, Jun. 07, 2017. doi: 10.48550/arXiv.1706.02413.

[54] K. Annadurai, “3D Shape Reconstruction from Multiple Range Image Views,” Master’s Thesis, The University of Waikato, New Zealand, 2006.

[55] P. Patias, T. B. Grivas, A. Kaspiris, C. Aggouris, and E. Drakoutos, “A review of the trunk surface metrics used as Scoliosis and other deformities evaluation indices,” *Scoliosis*, vol. 5, no. 1, p. 12, Jun. 2010, doi: 10.1186/1748-7161-5-12.

[56] X. Su, R. Dong, Z. Wen, and Y. Liu, “Reliability and Validity of Scoliosis Measurements Obtained with Surface Topography Techniques: A Systematic Review,” *J. Clin. Med.*, vol. 11, no. 23, Art. no. 23, Jan. 2022, doi: 10.3390/jcm11236998.

[57] M. Kazhdan, M. Bolitho, and H. Hoppe, *Poisson Surface Reconstruction*. The Eurographics Association, 2006. doi: 10.2312/SGP/SGP06/061-070.